Cavity-Enhanced Coherent Emission of Nitrogen-Vacancy Centers in Diamond

Master Thesis

Stijn Scheijen

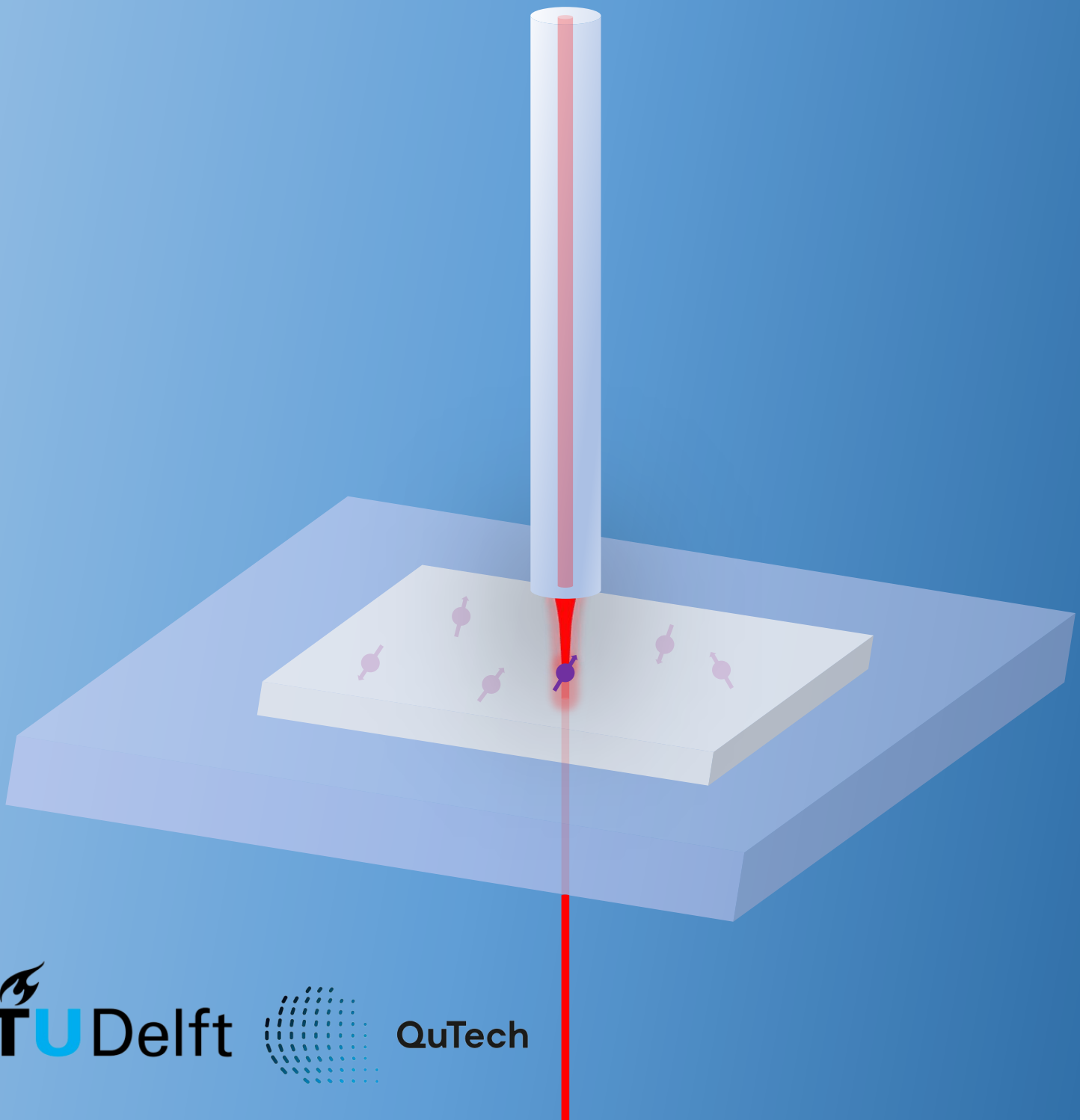

TU Delft QuTech

Cavity-Enhanced Coherent Emission of Nitrogen-Vacancy Centers in Diamond

Master Thesis

by

Stijn Scheijen

To obtain the degree of Master of Science
at the Delft University of Technology,
to be defended publicly on Wednesday February 7, 2024 at 13:00.

Thesis committee:	Prof. dr. ir. R. Hanson,	QuTech, Delft University of Technology
	Dr. ir. T. H. Taminiau,	QuTech, Delft University of Technology
	Prof. dr. ir. L. K. Kuipers,	Quantum Nanoscience, Delft University of Technology
Daily supervisor:	MSc. Y. S. Herrmann,	QuTech, Delft University of Technology

Abstract

The Nitrogen-Vacancy (NV) center has demonstrated great potential as a quantum networks platform. While many milestones have been reached, the current hardware implementations have reached their limit in terms of remote entanglement generation rates, which hinders the scalability of the platform. The most dominant limits are that only $\sim 3\%$ of the emission is coherent, and the outcoupling efficiency in state-of-the-art network experiments is $\sim 15\%$.

The coherent emission can be increased via the Purcell effect, which can be achieved by the use of an open Fabry-Pérot microcavity. In such a setup the NV center is embedded in a micrometer-thin diamond membrane, thereby retaining its favourable optical properties. The open microcavity has the ability of *in situ* spectral and spatial tunability. However, this is accompanied by a high susceptibility to vibrations, which needs to be considered in the experimental design. The goal of this thesis is to simultaneously increase the coherent emission and the outcoupling efficiency by coupling NV centers to an open Fabry-Pérot microcavity.

An optimized cavity is found by characterizing different fiber tip mirrors, reaching a bare cavity finesse of 9500. The vibrations in the bare cavity are analyzed, revealing a root mean square cavity length detuning of 22 pm while operating at low temperature.

A hybrid cavity is formed with a diamond membrane with NV centers, resulting in cavity with a finesse of 2100, quality factor of 266000, mode volume of 108 λ^3, and outcoupling efficiency $\sim 30\%$. Due to a different setup configuration, an increased root mean square cavity length detuning of 190 pm is measured, resulting in a lowered Purcell factor. Off-resonant measurements demonstrate the coupling of NV centers to the cavity. Moreover, excited state lifetimes are measured to obtain a Purcell factor of 2.6 ± 0.5, with a corresponding enhanced coherent emission ratio of 0.07 ± 0.01. This result is in good agreement with simulations that include the effect of vibrations. The ZPL branching ratio and outcoupling efficiency are improved by a factor two compared to state-of-the-art confocal microscope setups. For the first time in open microcavities, the ability to drive the spin of NV centers is shown by an optically detected magnetic resonance measurement with a contrast of $(28 \pm 2)\%$.

By improving the setup to the already obtained vibration level, and a realistic finesse of 5000, an expected Purcell factor of ~ 15.7 and outcoupling efficiency of $\sim 80\%$ can be reached, paving the way to the next-generation of quantum network nodes.

Acknowledgements

First of all, I would like to thank my daily supervisor Yanik. Your passion for the research that you do is infectious, and I learned a lot about this incredible field through our discussions. Working alongside you on the setup was an amazing experience. From anxiously watching each other handling the hero fiber, being stumped by the source of the increased vibrations, to finally coupling the first NV centers in the cavity, it truly felt like a roller coaster sometimes. Ronald, I would like to thank you for the opportunity of doing my thesis project in your group. I admire how you have cultivated such a fantastic and welcoming group that does incredible research, in which there is always room for humor. Julius, I am thankful that you always made time for my questions over a whiteboard discussion. Your energetic presence in the lab is truly contagious, and I will always remember the excitement we had over the genius 'NOS'-switch for the katana laser.

I want to thank Leo in particular for being an amazing master student colleague. Both lab and clean room work can be frustrating at times, but your banter always kept it light. I wish you good luck on your upcoming PhD adventure. Cees, I thank you for sharing the task of fiber characterization, and of course the countless Limburg jokes. I want to thank my fellow master students Pepijn, Joan, Caroline, Marit, Tobi, Hector, Alex and Constantijn for the fun and support in the master room, I wish you good luck on the remainder of your projects. Furthermore, I would like to thank everyone part of Team Diamond. I appreciate the way you welcomed me to your team, in both social and work-related settings.

I would like to express my gratitude to my parents Jo and Janine, as well as my sister Dionne, for their unwavering support over the years. I deeply appreciate your encouragement and involvement in my studies. Finally, I would like to thank my girlfriend Gina for her support, and for always patiently entertaining my conversations about quantum mechanics.

Contents

1

Introduction

A quantum internet [1, 2] will enable applications that are impossible with the classical internet, for example distributed quantum computation [3] and safe communication with quantum key distribution [4]. Such a network can be constructed with nodes consisting of an interface between solid state qubits with long coherence times and flying qubits that distribute quantum information.

A promising candidate for such nodes are color centers in diamond, the most researched being the negatively-charged nitrogen-vacancy (NV) center in diamond. NV centers offer optically addressable spin qubits with exceptional spin coherence times [5] that allow spin-photon entanglement [6]. Due to these favourable traits, the NV center has been the workhorse for quantum network research and many milestones have been reached, such as deterministic entanglement delivery between distant nodes [7], a multi-qubit quantum memory register [8] and a three-node network [9]. From these and many other experiments it is clear that the spin properties and readout fidelity of NV centers are excellent for quantum network applications. However, the entanglement rate and remote state fidelity need to be improved for practical applications. In particular, the experiments on the three-node network pushed the entanglement rates and state fidelity to the limit of the current state-of-the-art hardware. Therefore, the next step is to improve the hardware to increase these important parameters.

In order to distribute entanglement over the network, spin-spin entanglement of distant NV centers is generated by quantum interference schemes with the emitted photons of the NV centers [10]. This is accompanied by an intrinsic trade-off between the achievable entanglement rate and remote state fidelity. There are two schemes in use for entanglement generation: two photon interference [11] and one photon interference [12]. Two photon interference schemes require two photons to arrive at the same time. This makes them robust against infidelity induced by background noise, but also lowers the entanglement rate significantly [13]. While this is not necessary for single photon entanglement schemes, a trade-off between entanglement rate and state fidelity is made by choosing what spin-photon state is used, which fundamentally limits the achievable fidelity [7, 14].

Depending on the interference scheme that is used, the entanglement rate scales either linearly (single photon scheme) or quadratically (two photon scheme) with the probability of detecting a single photon after an optical excitation pulse [15]. Therefore, by increasing this probability, both the achievable entanglement rate and remote state fidelity are increased. The probability of detecting a coherent photon can be broken down as a product of probabilities, originating from the main causes of loss in the network, as shown in Figure 1.1.

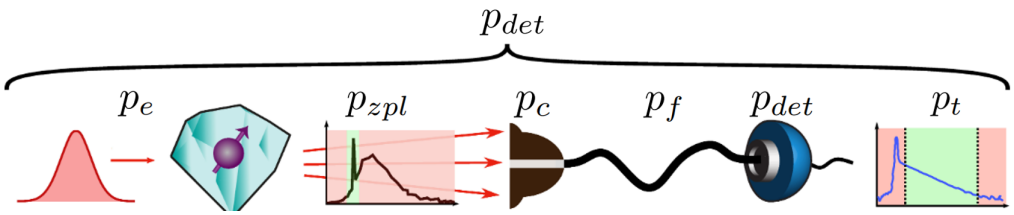

Figure 1.1: Probability of detecting a coherent photon after an optical excitation pulse. The NV center is excited by the optical pulse with probability p_e, before it decays coherently with probability p_{zpl}. The emitted photon is collected with outcoupling efficiency p_c. The photon is transmitted through the fiber with a success rate p_f before it is detected by the detector with efficiency p_{det}. The excitation pulse is filtered from the emission with an appropriate time window, which reduces the detection probability by p_t. Figure adapted from [15].

The focus of this thesis is on the probability that the NV center decays coherently (p_{zpl}) and the probability that the emitted photon is collected (p_c). The probability of coherent decay originates from the property that the NV center can radiatively decay in two ways: by emitting only one photon (zero phonon line emission, ZPL) or by emitting a lower energy photon accompanied by phonons (phonon sideband emission, PSB). Only the zero phonon line emission is useful for entanglement generation for two reasons. First, the quantum interference schemes used for entanglement generation require the photons from the NV centers to be indistinguishable. For phonon sideband emission the energy of the photon is not well-defined, which means that these photons can not be interfered. Second, with phonon-assisted decay, the phonon becomes entangled with the spin-photon state. This leaks information to the environment, causing the state to dephase [15]. The probability of coherent decay is given by the branching ratio into the ZPL of the NV center: $\beta_0 \approx 3\%$ [16].

The branching ratio into the ZPL can be increased with the Purcell effect. By embedding an NV center in an optical cavity whose resonance frequency matches the frequency of the ZPL emission, the spontaneous decay rate of the ZPL emission is increased [17, 18]. There are two main approaches for realizing Purcell enhancement for color centers in diamond: nanophotonic cavities and Fabry-Pérot microcavities.

Nanophotonic cavities are created by fabricating structures around an emitter that confine the electromagnetic field in its vicinity. Some examples are whispering gallery mode resonators, ring resonators and photonic crystal cavities [17]. Due to their small size, nanophotonic cavities confide the light in a very small volume, which increases the achievable Purcell enhancement. In addition, many nanophotonic cavities can be fabricated on a single sample and integrated with other photonics on a chip. However, the fabrication of these cavities is challenging, and the cavities lack tunability since many parameters are set by their geometry. More importantly, nanophotonic devices require compatible emitters. This is attributed to surface charges accumulating on the fabricated structures, which are in close proximity of the embedded emitter. The NV center is susceptible to the electric field produced by these surface charges due to its dipole structure, which causes broadening of the emission linewidth [19].

In order to retain the favourable optical properties of the NV center, in this thesis a Fabry-Pérot microcavity is implemented to obtain Purcell enhancement. These cavities are constructed by placing a diamond membrane with emitters on a plane mirror and positioning a spherical fiber tip mirror close to it. The resonance frequency of the cavity can be tuned by moving the fiber tip mirror closer or further from the plane mirror, and emitters can be chosen by moving the fiber to a different position on the sample. This *in situ* spectral and spatial tunability is accompanied by a high susceptibility to vibrations, which leads to cavity length changes. Therefore, experimental considerations have to be made to decrease the vibrations in the cavity.

The outcoupling efficiency p_c is limited by to the high refractive index of diamond. This causes refraction and total internal reflection, which inhibits collection of the emission. The approach to increase this in state-of-the-art network experiments is to fabricate a solid immersion lens around the emitter. This results in an outcoupling efficiency to $p_c \approx 15\%$ [20]. The outcoupling efficiency can be increased as well by placing the diamond membrane in a Fabry-Pérot microcavity, such that the emission is collected with a well-defined Gaussian beam.

The goal of this thesis is to simultaneously increase the branching ratio into the ZPL and the outcoupling efficiency of NV centers by coupling them to a Fabry-Pérot microcavity. The remainder of this thesis is structured as follows. In Chapter 2 the relevant theoretical background for NV centers and Fabry-Pérot cavities is discussed. This is followed by Chapter 3 where the experimental methods of the experiments are introduced. The fiber tip mirrors are characterized in Chapter 4, followed by the characterization of the bare cavity at low temperatures in Chapter 5. In Chapter 6 the experiments with the NV centers at low temperature are discussed. The conclusion and outlook of this thesis are given in Chapter 7.

2

Theory

In this chapter the theoretical background of the thesis is discussed. In the first section the relevant physical properties of the nitrogen-vacancy center in diamond are introduced. This is followed by a section on open Fabry-Pérot micro cavities, which includes the analysis and discussion on bare cavities and hybrid cavities. In the final section the Purcell enhancement of ZPL emission of the nitrogen-vacancy center in diamond is discussed.

2.1. Nitrogen-Vacancy Centers in Diamond

The nitrogen-vacancy (NV) center is a defect in diamond consisting of a nitrogen atom and a neighboring vacancy in the diamond crystal lattice (see Figure 2.1). In the neutral charge state (NV^0) the vacancy contains three electrons from neighboring carbon atoms and two electrons from the nitrogen atom [21]. In the negatively charged state (NV^-) an additional electron from a donor is present in the vacancy. In this thesis only the NV^- state is considered, which is referred to as the NV center.

The molecular orbitals with ground state occupancy of the NV center are shown in Figure 2.1. In the ground state the a_1' and a_1 orbitals are both doubly occupied and both the e_x and e_y are occupied by unpaired electrons. The excited state of the NV center is obtained by the promotion of one of the a_1 electrons to the e_x or e_y orbital, which changes the electron configuration from $a_1^2e^2$ to $a_1^1e^3$. These configurations are situated in the wide bandgap of diamond (5.5 eV) which shields the NV from it electronic environment, creating an ion-like system. In both the ground and excited state the two unpaired electrons have the lowest energy in the triplet state configuration ($S = 1$) as a result of Coulomb repulsion [22]. The Hamiltonian of the triplet ground state in the presence of a magnetic field is given by:

$$H_{gs} = D_{gs}\sigma_z^2 + \gamma_e \vec{B} \cdot \vec{S}, \tag{2.1}$$

where S_i are the Pauli spin operators, $D_{gs} = 2.88$ GHz is the zero-field splitting due to the spin-spin interaction and $\gamma_e = 2\pi \times 2.802$ MHz/G the electron gyromagnetic ratio. Without the presence of a magnetic field the $m_s = 0$ and $m_s = \pm 1$ states are split by D_{gs}. Applying a magnetic field lifts the degeneracy of the $m_s = \pm 1$ states in accordance with the gyromagnetic ratio γ_e due to the Zeeman effect. A detailed overview of the electronic structure of the NV center is given in Figure 2.2.

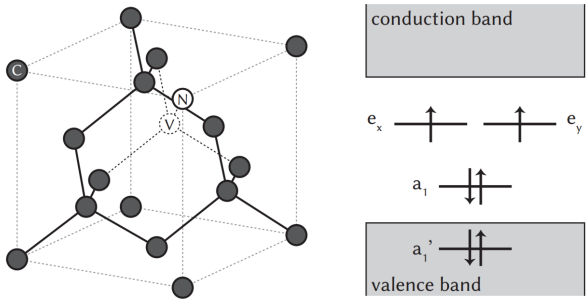

Figure 2.1: Structure of the NV center. Left: Schematic view of the crystal structure of a nitrogen-vacancy in diamond. In the NV^- state the vacancy is occupied by three electrons from carbon atoms, two from the nitrogen atom and one from a donor in the environment. **Right:** Molecular orbitals of NV^- with ground state occupancy in accordance with Pauli's exclusion principle. The excited state is obtained by the promotion of one of the a_1 electrons to the e_x or e_y orbital. Figure adapted from [21].

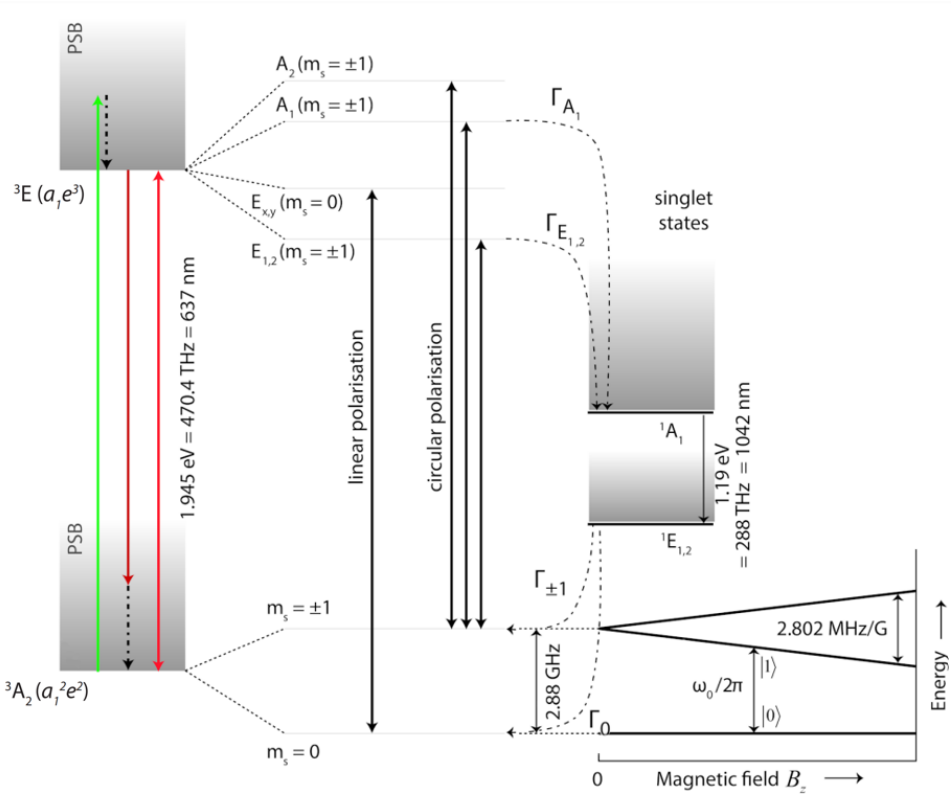

Figure 2.2: Electronic structure of the NV center. The excited state can decay to through the ZPL (red arrow) or the PSB (dark red arrow). Similarly, the ground state can be excited through the resonant excitation (red arrow) or by off-resonant excitation (green arrow). The optical transitions are mostly spin-preserving, except for the decay through the singlet states (dotted lines). Applying a magnetic field lifts the degeneracy of the $m_s = \pm 1$ states which enables the definition of a qubit between the $m_s = 0$ ($|0\rangle$) and $m_s = -1$ or $m_s = 1$ ($|1\rangle$) states. Figure adapted from [21]

The ground state ($^3A_2$) and excited state (^3E) are split by 1.945 eV, which corresponds to a photon wavelength of 637 nm. The excited state can decay to the ground state by zero-phonon line (ZPL) emission by emitting a single photon with $\lambda = 637$ nm, or by phonon sideband (PSB) emission by emitting a photon with $\lambda > 637$ nm accompanied by the excitation of one or multiple phonons. Similarly, the NV center can be excited resonantly with light of $\lambda = 637$ nm, or off-resonantly with light of $\lambda < 637$ nm and the excitation of phonons.

The PSB emission of the NV center is not well-defined in frequency, as shown in Figure 2.3. For this reason, in addition to phonon-induced dephasing, only the ZPL emission can be used as a source of

indistinguishable photons for entangling schemes [15]. The branching ratio of emission into the ZPL is determined by the Debye-Waller factor $\beta_0 \approx 3\%$ [16]. The main arguments of coupling the NV center to an optical cavity is to increase this emission ratio and the photon collection efficiency, this is further discussed in Section 2.3.

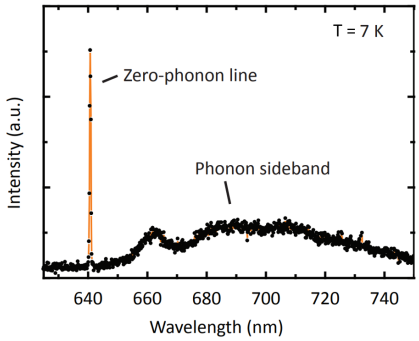

Figure 2.3: Emission spectrum of the NV center. The spectrum is taken at $T = 7$ K. At this temperature the ZPL is narrow while the PSB is very broad. Figure adapted from [23].

The qubit is defined by the states $m_s = 0$ ($|0\rangle$) and $m_s = -1$ or $m_s = 1$ ($|1\rangle$). The energy splitting of the $|0\rangle$ and $|1\rangle$ states is in the GHz range, thus the qubit can be manipulated with microwave pulses. The initialization and readout of the qubit is done with spin-selective optical transitions of the NV center. This is possible because the optical transitions are mostly spin preserving, except for decay through the singlet states [21].

2.2. Open Fabry-Pérot Microcavities

The goal of this thesis is to couple a NV center to an open Fabry-Pérot microcavity to obtain Purcell enhancement in ZPL emission. The open microcavity considered in this thesis is constructed with a plane superpolished mirror and a fiber tip mirror. In this section the physics regarding open Fabry-Pérot microcavities is discussed. In section 2.2.1 some important parameters of bare open microcavities are obtained with the use of a one-dimensional model. This includes the resonance condition, finesse, cavity linewidth and free spectral range. In section 2.2.2 the mode structure of the light in a three-dimensional bare cavity is discussed. Once the bare cavity is analyzed the hybrid cavity is introduced with a similar structure. In section 2.2.3 some additional parameters are defined that are relevant for hybrid microcavities and in section 2.2.4 the mode structure of the light in a three-dimensional hybrid cavity is discussed.

2.2.1. One-dimensional model of a bare cavity

In this section the parameters that characterize a bare Fabry-Pérot cavity are obtained with the use of the transfer-matrix method on a one-dimensional model [22]. The goal is to construct a transfer matrix that describes the relation between the incident, reflected and transmitted electric field such that:

$$\begin{pmatrix} E_{in} \\ E_{refl} \end{pmatrix} = M_{cav} \begin{pmatrix} E_{trans} \\ 0 \end{pmatrix}. \tag{2.2}$$

The model consists of two mirrors separated by a distance of L_{cav}, see Figure(2.4). The mirrors are represented by the transfer matrices:

$$M_i = \frac{1}{t_i} \begin{pmatrix} 1 & r_i \\ r_i & 1 \end{pmatrix}, \tag{2.3}$$

where t_i and r_i are the transmission and reflection coefficients of mirror $i = 1, 2$. The propagation of light between the mirrors over a distance L_{cav} in a medium with refractive index n is represented by:

$$P = \begin{pmatrix} e^{ikL_{cav}} & 0 \\ 0 & e^{-ikL_{cav}} \end{pmatrix}, \tag{2.4}$$

where $k = 2\pi n/\lambda_0$ is the wavenumber of the light inside the cavity. The total transfer matrix of the cavity is obtained by multiplication of the individual transfer matrices, which results in:

$$\begin{aligned} M_{cav} &= M_2 P M_1 \\ &= \frac{1}{t_2} \begin{pmatrix} 1 & r_2 \\ r_2 & 1 \end{pmatrix} \begin{pmatrix} e^{ikL_{cav}} & 0 \\ 0 & e^{-ikL_{cav}} \end{pmatrix} \frac{1}{t_1} \begin{pmatrix} 1 & -r_1 \\ -r_1 & 1 \end{pmatrix} \\ &= \frac{1}{t_1 t_2} \begin{pmatrix} e^{ikL_{cav}} - r_1 r_2 e^{-ikL_{cav}} & -r_1 e^{ikL_{cav}} + r_2 e^{-ikL_{cav}} \\ r_2 e^{ikL_{cav}} - r_1 e^{-ikL_{cav}} & e^{ikL_{cav}} - r_1 r_2 e^{-ikL_{cav}} \end{pmatrix}. \end{aligned} \tag{2.5}$$

By combining Eq.(2.2) and Eq.(2.5) the transmittance of the cavity T is calculated:

$$\begin{aligned} T &= \left| \frac{E_{trans}}{E_{in}} \right|^2 = \left| \frac{1}{M_{cav[1,1]}} \right|^2 = \frac{|t_1|^2 |t_2|^2}{\left| e^{ikL_{cav}} - r_1 r_2 e^{-ikL_{cav}} \right|^2} \\ &= \frac{|t_1|^2 |t_2|^2}{(1 - r_1 r_2)^2 \left(1 + \left(2 \frac{\sqrt{r_1 r_2}}{1 - r_1 r_2} \right)^2 \sin^2(kL_{cav}) \right)} \\ &= \frac{|t_1|^2 |t_2|^2}{(1 - r_1 r_2)^2 \left(1 + \left(\frac{2\mathcal{F}}{\pi} \right)^2 \sin^2(kL_{cav}) \right)}, \end{aligned} \tag{2.6}$$

where in the last step the finesse is defined as:

$$\mathcal{F} \equiv \frac{\pi \sqrt{r_1 r_2}}{1 - r_1 r_2} \approx \frac{2\pi}{\mathcal{L}_{tot}}, \tag{2.7}$$

where $\mathcal{L}_{tot} = \mathcal{L}_1 + \mathcal{L}_2$ are the total losses in the cavity, with $\mathcal{L}_i$ the losses of mirror $i = 1, 2$. The approximation in Eq. (2.7) is valid for mirrors with high reflectivity such that $r_i \approx \sqrt{1 - \mathcal{L}}$, which is the case for all mirrors considered in this thesis. Any additional losses present in the cavity are added to the denominator of Eq.(2.7). The finesse is a measure of the number of round-trips light makes before it is lost from the cavity. Therefore, this is an important parameter which quantifies the quality of an optical cavity.

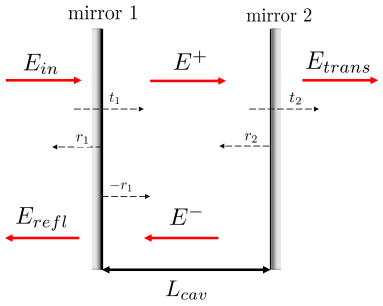

Figure 2.4: One-dimensional model of a Fabry-Pérot cavity The model consists of two mirrors with a reflectivity coefficient of r_1 and r_2 separated by a distance of L_{cav}.

From Eq.(2.6) the resonance condition of the cavity is obtained by calculating the cavity length for maximum transmission:

$$kL_{cav} = m\pi \rightarrow L_{cav} = \frac{m\pi}{k} = m\frac{\lambda}{2} = m\frac{c}{2n\nu}, \quad \text{with} \quad m \in \mathbb{N}, \tag{2.8}$$

which arises from the constructive interference of the electromagnetic field every multiple of $\lambda/2$. From this equation the frequency separation of subsequent modes is found, which is called the free spectral range (FSR):

$$\nu_{FSR} = \frac{c}{2nL_{cav}}. \tag{2.9}$$

In addition, Eq.(2.6) is used to determine the cavity linewidth $\delta\nu$, which is defined as the full width at half maximum (FWHM) of the transmitted light. An alternative definition of the linewidth is $\delta\nu = \kappa/2\pi$, where $\kappa = \frac{\text{losses per round-trip}}{\text{round-trip duration}}$ is the decay rate of the cavity. The linewidth is determined by finding $\delta\nu$ for which $T(\nu_{res} + \delta\nu/2) = T_{max}/2$, which is valid for:

$$1 + \left(\frac{2\mathcal{F}}{\pi}\right)^2 \sin^2(kL_{cav}) = 2 \rightarrow \sin(2\pi n(\nu_{res} + \delta\nu/2)L_{cav}/c) = \frac{\pi}{2\mathcal{F}}. \tag{2.10}$$

The linewidth is obtained by making use of the small angle approximation and $\sin(k_{res}L_{cav}) = 0$:

$$\sin(\pi n\delta\nu L_{cav}/c) \approx \pi n\delta\nu L_{cav}/c = \frac{\pi}{2\mathcal{F}} \rightarrow \delta\nu = \frac{c}{2nL_{cav}\mathcal{F}}. \tag{2.11}$$

By combining Eq.(2.9) and Eq.(2.11), the finesse can be defined as:

$$\mathcal{F} = \frac{\nu_{FSR}}{\delta\nu}. \tag{2.12}$$

This is an important result since this formulation provides a method to obtain the finesse experimentally by measuring the FSR and linewidth of a cavity. Another metric used to quantify the quality of a cavity is the quality factor, which is defined as:

$$Q = \frac{\nu}{\delta\nu}. \tag{2.13}$$

The quality factor represents the number of optical cycles a field in the cavity undergoes until its energy is reduced to $1/e$ of its initial value, and this is related to the finesse by $Q = (\nu/\nu_{FSR})\mathcal{F}$. The main difference between the two metrics is that the quality factor depends on the length of the cavity, while the finesse does not. For this reason is the quality factor mainly used in literature for nanophotonic crystal cavities since these have a fixed cavity length, while the finesse is used for tunable open micro-cavities.

2.2.2. Resonant modes in a bare plane-concave cavity

While the one-dimensional model of the previous sections gives insight in the parameters that characterize a cavity, the three-dimensional geometry has to be considered to understand the structure of the modes inside the cavity. The cavities considered in this thesis consist of a plane mirror and a spherical mirror with radius of convergence ROC, separated by a distance L_{cav} in a medium with refractive index n (see Figure (2.5)). The complex amplitude $U(\mathbf{r})$ of the cavity mode obeys the Helmholtz equation [24]:

$$\nabla^2 U + k^2 U = 0. \tag{2.14}$$

By assuming that the angle between normal of the wavefronts and the z-axis is small, the paraxial approximation is used:

$$U(\mathbf{r}) = A(\mathbf{r}) e^{-ikz}. \tag{2.15}$$

The wavefronts of the cavity mode must follow the shape of the two mirrors to have a resonant mode. A solution that obeys this condition is the Gaussian beam [25]:

$$\begin{aligned} U(\mathbf{r}) &= \frac{A_1}{q(z)} \exp\left(-ik\frac{\rho^2}{2q(z)}\right)\exp(-ikz) \\ &= A_0 \frac{w_0}{W(z)} \exp\left(-\frac{\rho^2}{W^2(z)}\right)\exp\left(-ikz - ik\frac{\rho^2}{2R(z)} + i\zeta(z)\right); \end{aligned} \tag{2.16}$$

$$W(z) = w_0\sqrt{1 + (z/z_0)^2}; \tag{2.17}$$

$$R(z) = z\left(1 + (z_0/z)^2\right); \tag{2.18}$$

$$\zeta(z) = \arctan(z/z_0); \tag{2.19}$$

$$w_0 = \sqrt{\frac{\lambda_0 z_0}{n\pi}}, \tag{2.20}$$

where ρ is the radial coordinate, z_0 the Rayleigh range, w_0 the beam waist and $\zeta(z)$ the Gouy phase. In this expression the complex beam parameter $q(z) = z + iz_0 = z + i(\pi n w_0^2/\lambda_0)$ is rewritten to show the beam width $W(z)$ and radius of curvature of the wave front $R(z)$ explicitly in the equation, resulting in:

$$1/q(z) = 1/R(z) - i(\lambda_0/\pi n W^2(z)). \tag{2.21}$$

A schematic view of the Gaussian cavity mode is given in Figure 2.5. The beam waist w_0 is the minimal radius of the beam and the Rayleigh range z_0 is the longitudinal coordinate where $R(z)$ is minimal. The boundary conditions arising from the geometry of the cavity are $W(0) = w_0$, $R(0) \to \infty$ and $R(L_{cav}) = ROC$. With these conditions the beam waist can be written as:

$$w_0 = \sqrt{\lambda_0/\pi}\sqrt[4]{L_{cav}(ROC - L_{cav})}. \tag{2.22}$$

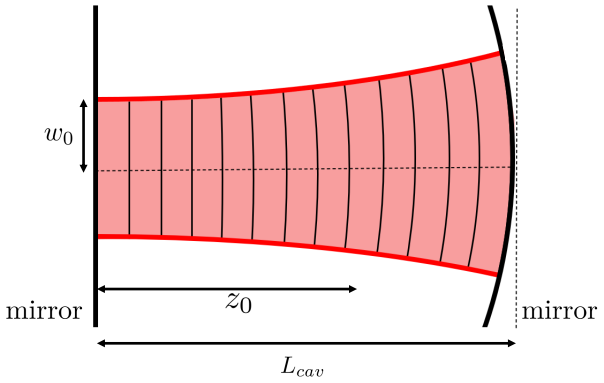

Figure 2.5: Schematic view of the cavity mode. The wavefronts at the boundaries match the shape of the mirrors of the cavity. The beam waist $W(z)$ is minimal for $z = 0$ and the ROC is minimal for $z = z_0$.

While the Gaussian mode is a solution to Eq.(2.14) with the boundary conditions of the plane-concave cavity, this is only the simplest form of a set of orthogonal solutions, called the Hermite-Gauss modes. These modes have characteristic intensity profiles, some examples are shown in Figure 2.6. A Hermite-Gauss mode of order (m, n) is described by:

$$\begin{aligned} U_{m,n}(\mathbf{r}) =& A_0 \frac{w_0}{W(z)} H_m\left(\frac{\sqrt{2}x}{W(z)}\right) \exp\left(-\frac{x^2}{W(z)^2}\right) H_n\left(\frac{\sqrt{2}y}{W(z)}\right) \times \\ & \exp\left(-\frac{x^2}{W(z)^2}\right) \exp\left(-ikz - ik\frac{x^2+y^2}{2R(z)} + i\zeta(z)\right), \end{aligned} \tag{2.23}$$

where $\zeta(z) = (1 + m + n) \arctan(z/z_0)$ is the Gouy phase and H_m is the Hermite polynomial of degree m [22]. Since the Gouy phase depends on the order of the mode, the frequency of each mode is shifted. The frequency of a Hermite-Gauss mode of order (n, m) is given by [26]:

$$\begin{aligned} \nu_{m,n} = \frac{c}{4\pi L_{cav}} \Bigg(& 2\pi k + (2m+1) \arccos\left(\sqrt{1 - L_{cav}/ROC_x}\right) \\ & + (2n+1) \arccos\left(\sqrt{1 - L_{cav}/ROC_y}\right) \Bigg), \end{aligned} \tag{2.24}$$

where ROC_x and ROC_y are the radii of curvature in x- and y-direction of the spherical mirror. This indicates that for a perfect spherical mirror the frequency of the modes of total order $\tilde{m} = m + n$ are the same, but for a mirror with a non-zero ellipticity the frequencies are split. For the remainder of this thesis the Gaussian mode is referred to as the fundamental mode.

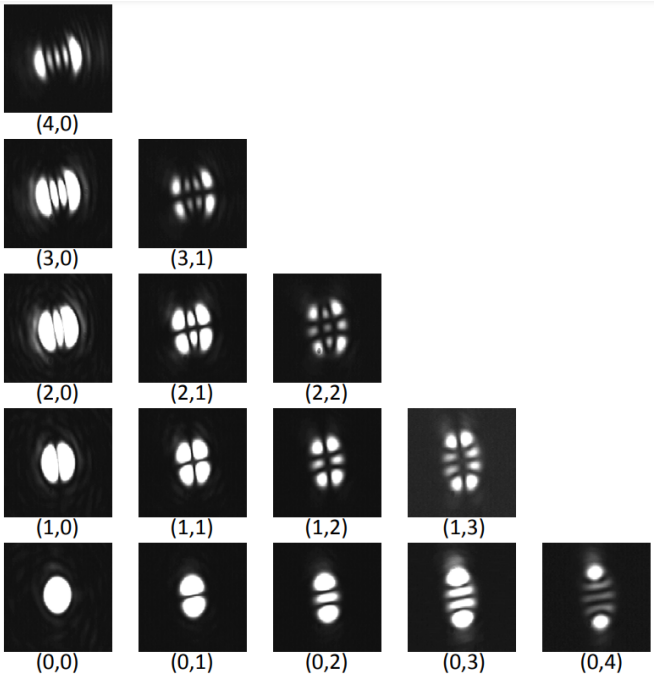

Figure 2.6: Intensity profile of Hermite-Gauss modes. The characteristic beam intensity profile of the Gaussian mode $(0, 0)$ and higher order modes. Labels indicate the order of the mode (n, m). Image adapted from [22].

2.2.3. One-dimensional model of a hybrid cavity

The NV centers considered in this thesis are embedded in diamond membranes. The NV centers are coupled to the cavity by bonding the diamond membrane to the plane mirror of the cavity with van der Waals forces. The high refractive index of diamond ($n_d = 2.41$) introduces changes to the properties of the microcavity, which are analysed in this section with the use of a one-dimensional model.

The model consists of two mirrors with the same reflection and transmission coefficients r and t, separated by a distance $L_{cav} = t_d + t_a$, where t_d is the the thickness of the diamond membrane and t_a is width of the air gap. In addition to the transfer matrices introduced in section 2.2.1, the transition between diamond and air is described with [22]:

$$I_{d\to a} = \frac{1}{1+r_d}\begin{pmatrix} 1 & r_d \\ r_d & 1 \end{pmatrix}, \quad I_{a\to d} = \frac{1}{1-r_d}\begin{pmatrix} 1 & -r_d \\ -r_d & 1 \end{pmatrix}, \tag{2.25}$$

where $r_d = \frac{n_a - n_d}{n_a + n_d}$. This results in the total transfer matrix:

$$\begin{aligned} M_{cav} &= M_2 P_a I_{d\to a} P_d I_{a\to d} M_1 \\ &= \frac{1}{t}\begin{pmatrix} 1 & r \\ r & 1 \end{pmatrix}\begin{pmatrix} e^{ik_a t_a} & 0 \\ 0 & e^{-ik_a t_a} \end{pmatrix}\frac{1}{1+r_d}\begin{pmatrix} 1 & r_d \\ r_d & 1 \end{pmatrix}\begin{pmatrix} e^{ik_d t_d} & 0 \\ 0 & e^{-ik_d t_d} \end{pmatrix}\times \\ &\frac{1}{1-r_d}\begin{pmatrix} 1 & -r_d \\ -r_d & 1 \end{pmatrix}\frac{1}{t}\begin{pmatrix} 1 & -r \\ -r & 1 \end{pmatrix}, \end{aligned} \tag{2.26}$$

where $k_a = 2\pi n_a \nu/c$ and $k_d = 2\pi n_d \nu/c$ are the wavenumbers in air and diamond respectively. The transmittance is obtained in a similar manner to that of the bare cavity ($T = 1/|M_{[1,1]}|^2$), which gives:

$$T = \frac{|(r_d - n_a)t^2|^2}{|1 - e^{2ik_a(n_a t_a + n_d t_d)} + r_d(e^{-2ik_a n_a t_a} - e^{-2ik_d n_d t_d})|^2}. \tag{2.27}$$

From this the resonance condition is obtained:

$$(n_a + n_d)\sin\left(\frac{2\pi\nu}{c}(n_a t_a + n_d t_d)\right) = (n_a - n_d)\sin\left(\frac{2\pi\nu}{c}(n_a t_a - n_d t_d)\right). \tag{2.28}$$

The resonance frequencies ν_m are approximated by writing them as a deviation $\Delta\nu_{ad}$ from the resonance frequencies of the bare cavity ($\nu_m = mc/2(n_a t_a + n_d t_d) + \Delta\nu_{ad}$). This is solved by neglecting $\Delta\nu_{ad}$ the right hand side of Eq. (2.28) [27]:

$$\nu_m \approx \frac{c}{2\pi(n_a t_a + n_d t_d)}\left(m\pi - (-1)^m \arcsin\left(\frac{n_d - n_a}{n_d + n_a}\sin\left(\pi m \frac{n_a t_a - n_d t_d}{n_a t_a + n_d t_d}\right)\right)\right). \tag{2.29}$$

There are two type of modes for which the oscillating term of Eq.(2.29) vanishes, these are the 'air-like modes' in which the mode has an antinode at the diamond-air interface, and the 'diamond-like modes' in which the mode has an node at the diamond-air interface. These conditions are satisfied for [18]:

$$t_d = m_d\frac{\lambda_0}{2n_d} \quad \text{and} \quad t_a = m_a\frac{\lambda_0}{2n_a}; \qquad (\textit{air-like mode}) \tag{2.30}$$

$$t_d = (2m_d + 1)\frac{\lambda_0}{4n_d} \quad \text{and} \quad t_a = (2m_a - 1)\frac{\lambda_0}{4n_a}, \qquad (\textit{diamond-like mode}) \tag{2.31}$$

where m_a and m_d are the number of antinodes in air and diamond respectively. The spectrum of resonant modes of the hybrid cavity is given in Figure 2.7.

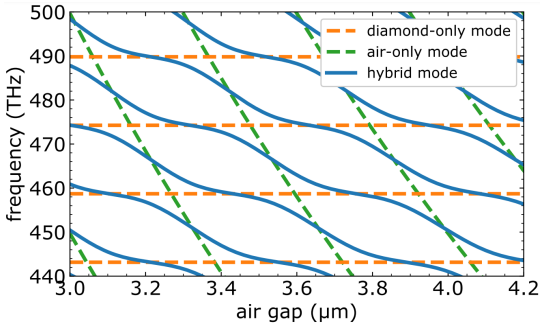

Figure 2.7: Resonance frequencies of a hybrid cavity. The hybrid modes in a hybrid cavity (blue) follow the fundamental mode spectrum for varying cavity length according to Eq.(2.29). The air-only (green) and diamond-only (orange) modes show the mode structure for a cavity consisting of only air or diamond. The diamond-like and air-like modes occur at the intersections of the hybrid modes and the diamond-only and air-only modes respectively. Figure adapted from [18].

The electric field distribution within the hybrid cavity can be calculated numerically with use of the transfer matrix model. To do this, the mirror matrices M_1 and M_2 of Eq.(2.26) are substituted with layers of propagation matrices with alternating refractive indices, representing distributed Bragg mirror coatings. The amplitude of the electric field can be calculated at each distance z by the applying relevant matrices for z, starting from the right-hand side, assuming there is no backwards propagating field. An example of the electric field distribution for air-like and diamond-like mode in a hybrid cavity is given in Figure 2.8.

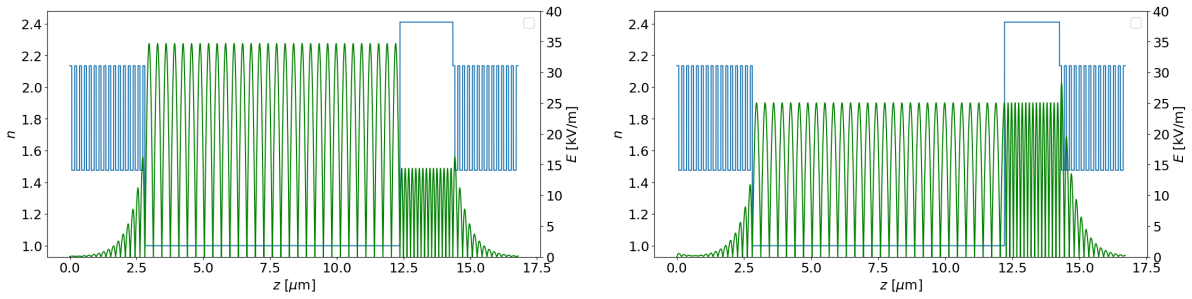

Figure 2.8: Electric field distribution of air-like and diamond-like modes in a hybrid cavity. The electric field distribution (green) of both air-like (left) and diamond-like (right) modes are simulated using the transfer matrix method for a diamond thickness of $t_d \approx 2$ µm and air length $t_a \approx 9$ µm. The refractive index (blue) of the distributed Bragg mirrors are simulated as alternating layers of Ta_2O_5 ($n = 2.14$) and SiO_2 ($n = 1.48$).

Figure 2.7 and 2.8 show that the fundamental mode spectrum and electric field distribution highly depend on the type of mode the cavity supports. The intensity at the NV center is greater for diamond-like modes compared to air-like modes. Moreover, diamond-like modes are much more resilient against vibrations because the slope of the dispersion relation between resonance frequency and air gap is more shallow (see Figure 2.7). However, the scattering losses from the diamond are a lot higher, since diamond-like modes have an anti-node at the diamond-air interface. Therefore, diamond-like modes require very high diamond surface quality to obtain a high finesse.

The total losses of the hybrid cavity are:

$$\mathcal{L}_{tot} = \mathcal{L}_{plane} + \mathcal{L}_{fiber} + \mathcal{L}_{diamond} + \mathcal{L}_{clip}, \tag{2.32}$$

where $\mathcal{L}_{plane}$ and $\mathcal{L}_{fiber}$ are the losses of the mirrors, $\mathcal{L}_{diamond}$ the losses at the diamond-air surface and $\mathcal{L}_{clip}$ the losses due to clipping. The losses at the diamond-air interface are due to scattering and absorption of photons. These losses can be minimized by fabricating the diamond sample with very low surface roughness and operating the cavity in an air-like mode. Clipping losses occur when the beam width on the dimple is larger than the spherical region of the concave mirror. The part of the beam

outside of the spherical region does not match the shape of the mirror, and is therefore lost from the cavity. Clipping losses are easily avoided by making the cavity length sufficiently small, but can also be implemented by making the cavity length larger when a measurement requires a low finesse, such as the vibration measurements discussed in Section 5.1. The total losses can be used to calculate the outcoupling efficiency of the cavity. By assuming that all the light that is lost by the plane mirror is collected with the objective, the outcoupling efficiency is calculated with:

$$\text{Outcoupling efficiency} = \frac{\mathcal{L}_{plane}}{\mathcal{L}_{tot}}. \tag{2.33}$$

This is a reasonable assumption since the light exits the cavity in a well-defined Gaussian beam. The mode structure inside the hybrid cavity is discussed in the next section.

2.2.4. Gaussian Beams in a Hybrid Cavity

In this section the structure of the resonant modes inside a hybrid cavity are discussed. In contrast with a bare cavity, a hybrid cavity no longer has an homogeneous refractive index. Since the structure of a Gaussian beam depends on the refractive index of the material it resides in (see Section 2.2.2), the mode inside the hybrid cavity is no longer defined as one Gaussian beam. Instead, the mode is defined by two Gaussian beams, one residing in air and the other in diamond. The respective beam waists of the modes are [18]:

$$w_{0,a} = \sqrt{\frac{\lambda_0 z_{0,a}}{n_a \pi}}, \quad w_{0,d} = \sqrt{\frac{\lambda_0 z_{0,d}}{n_d \pi}}, \tag{2.34}$$

where $z_{0,a}$ and $z_{0,d}$ are the Rayleigh ranges in air and diamond respectively. As the diamond is bonded to the plane mirror, the beam waist of the diamond beam is fixed at $z = 0$. The beam waist of the air beam is at some distance Δz_a. This gives an expression for the beam width and radius of curvature of the modes [22]:

$$W_a(z) = w_{0,a}\sqrt{1 + (z - \Delta z_a/z_{0,a})^2}, \quad W_d(z) = w_{0,d}\sqrt{1 + (z/z_{0,d})^2}, \tag{2.35}$$

$$R_a(z) = (z - \Delta z_a)\Big(1 + (z_{0,a}/(z - \Delta z_a))^2\Big), \quad R_d(z) = z\Big(1 + (z_{0,d}/z)^2\Big). \tag{2.36}$$

The transformation of the complex beam parameter q at the diamond-air interface can be found with use of the 'ABCD-matrix' law [28]:

$$q_d = \frac{Aq_a + B}{Cq_a + D} = \frac{n_d}{n_a} q_a, \tag{2.37}$$

where $A = 1, B = C = 0$ and $D = n_a/n_d$ are the matrix elements for refraction as defined for a paraxial ray. By combining Eq.(2.21) and Eq.(2.37) the following boundary conditions at the interface are obtained:

$$n_d R_a(t_d) = n_a R_d(t_d), \tag{2.38}$$

$$W_a(t_d) = W_d(t_d), \tag{2.39}$$

which can be solved to give:

$$w_{0,a} = w_{0,d} \equiv w_0, \tag{2.40}$$

$$\Delta z_a = t_d(1 - n_a/n_d). \tag{2.41}$$

Combining this with the boundary condition imposed by the spherical mirror $R_a(t_a + t_d) = ROC$ gives an expression for the beam width inside the hybrid cavity:

$$w_0 = \sqrt{\frac{\lambda_0}{\pi n_a}} \sqrt[4]{\left(t_a + \frac{n_a t_d}{n_d}\right)\left(ROC - \left(t_a + \frac{n_a t_d}{n_d}\right)\right)}, \tag{2.42}$$

which is the same expression as the beam waist for a bare cavity (Eq.(2.22)) with $L_{cav} \to t_a + \frac{n_a t_d}{n_d} \equiv L'$.

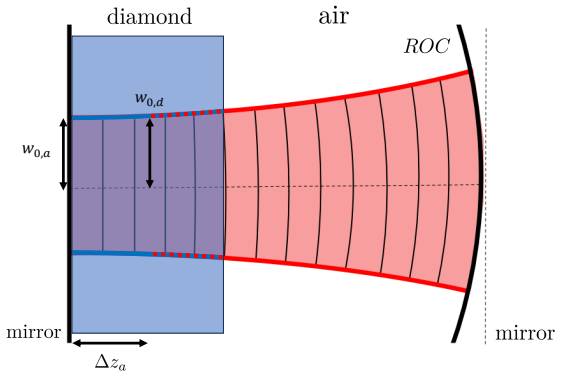

Figure 2.9: Schematic view of a hybrid cavity. The mode in the hybrid cavity is defined as two Gaussian beams, one residing in diamond (blue) and the other one in air (red). The beam waist of the diamond Gaussian is positioned at the plane mirror and the beam waist of the air Gaussian is positioned at a distance Δz_a from the plane mirror.

With the beam waist and the electric field distribution (see Section 2.2.3), the mode volume V_0 can be calculated, which is an important parameter for the spontaneous emission rate of a quantum emitter (further discussed in Section 2.3.1). The mode volume of a Gaussian beam in a cavity is given by [18]:

$$V_0 = \frac{\int_{cav} \epsilon(\vec{r})|\vec{E}(\vec{r})|^2 d^3\vec{r}}{\epsilon(\vec{r}_{NV}))|E(\vec{r}_{NV})|^2} = \frac{\pi\omega_0^2}{2} \frac{\int_{cav} \epsilon(\vec{r})|\vec{E}(\vec{r})|^2 dz}{\epsilon(\vec{r}_{NV}))|E(\vec{r}_{NV})|^2}, \tag{2.43}$$

with the assumption that the position of the NV center $\vec{r}_{NV}$ is on an antinode of the electric field in the diamond. From this expression the effective length is defined:

$$L_{eff} = \frac{\int_{cav} \epsilon(\vec{r})|\vec{E}(\vec{r})|^2 dz}{\epsilon(\vec{r}_{NV}))|E(\vec{r}_{NV})|^2}. \tag{2.44}$$

This is an important parameter since the absolute length of the cavity L_{cav} has no direct relation to the linewidth of the cavity, as this is defined as $\delta\nu = \kappa/2\pi$, with $\kappa = \frac{\text{losses per round-trip}}{\text{round-trip duration}} = \frac{\mathcal{L}}{2nL_{cav}/c}$. The problem with this formulation is that a 'round-trip' is no longer defined, since the diamond-air interface is partially reflective. Therefore, the round-trip length is defined as two times the effective length, resulting in an expression for the linewidth analogous to Eq.(2.11):

$$\delta\nu = \frac{c/2n_d(2L_{eff})}{2\pi/\mathcal{L}_{eff}} \quad \rightarrow \quad \mathcal{F} = \frac{2\pi}{\mathcal{L}_{eff}}, \tag{2.45}$$

where $\mathcal{L}_{eff}$ are the total losses during an effective round-trip. Consequently, the finesse of a hybrid cavity can be obtained experimentally. This is done by measuring the linewidth and calculating the effective length with the measured diamond thickness and air gap.

2.3. Purcell Enhancement of NV Centers in Optical Cavities

In this section the Purcell enhancement of the ZPL emission of NV centers is discussed. First, the physics of spontaneous emission of general quantum emitters is discussed to reveal the relevant parameters of transition rates. This is followed by a section on how these parameters can be adjusted to increase the ZPL emission rate of NV centers.

2.3.1. Transition Rates of Quantum Emitters

According to quantum mechanics, the probability of a state $|i\rangle$ subject to a Hamiltonian H transitioning to the state $|f\rangle$ is zero. Transitions between a systems eigenstates are only possible due to a perturbation of the Hamiltonian. In the case of spontaneous emission, this perturbation originates from the fluctuations of the vacuum field. The rate at which spontaneous emission is given by Fermi's golden rule [29]:

$$\Gamma_{i\to f} = \frac{2\pi}{\hbar} \left|\langle f_k|H_{int}|i\rangle\right|^2 D(\omega_k), \tag{2.46}$$

where H_{int} is the interaction term between the electron and the vacuum field and $D(\omega_k)$ the density of photon states of frequency ω_k. The initial state is the product state of the excited emitter and no photon present ($|i\rangle = |e\rangle \otimes |0\rangle$) and the final state is the product state of the emitter in the ground state and a photon present with wavevector k ($|f\rangle = |g\rangle \otimes |1_k\rangle$). Within the dipole approximation the interaction Hamiltonian is $H_{int} = \vec{d} \cdot \vec{E}$, which leads to a spontaneous emission rate of:

$$\Gamma_{i\to f} = \frac{\pi\omega}{\hbar\epsilon_0 V_0}\mu_{ge}^2 |\hat{d}\cdot\hat{e}|^2 D(\omega), \tag{2.47}$$

where $\hat{d}$ is the orientation of the electric dipole moment, $\hat{e}$ the electric field polarisation, $\mu_{eg}\hat{d} = \langle g|\hat{d}|e\rangle$ the transition matrix element and V_0 the mode volume. The density of photon states in free space is given by [22]:

$$D(\omega) = \frac{\omega_k^2 V_0 n^3}{\pi c^3}, \tag{2.48}$$

where n is the refractive index in which the emitter is embedded. The spontaneous emission rate of emitters can be enhanced for photons of specific wavelengths by altering the density of states with the use of optical cavities, this is further discussed in the next section.

2.3.2. Purcell Enhancement of NV Centers

As previously discussed in Section 2.1, the NV center decays radiatively in the ZPL and the PSB, while only the ZPL emission is useful for entanglement generation. The total decay rate of the NV center is the sum of these rates: $\Gamma_{tot} = \Gamma_{ZPL} + \Gamma_{PSB}$. Therefore, the branching ratio of ZPL emission is:

$$\beta_0 = \frac{\Gamma_{ZPL}}{\Gamma_{ZPL} + \Gamma_{PSB}}, \tag{2.49}$$

which is approximately 3% for the NV center in diamond [16]. This ratio can be increased by altering the density of states such that it is increased for ν_{ZPL}. In this thesis this is achieved with the use of an open Fabry-Pérot microcavity.

As discussed in Section 2.2, the frequency spectrum of an optical cavity consists of resonance peaks with a linewidth of $\delta\nu = \kappa/2\pi$. The resonance peaks are spaced apart by ν_{FSR} for a bare cavity or according to Eq.(2.29) for a hybrid cavity. The density of states in the cavity follows the same pattern, but normalized such that for each mode the total density is equal to unity, see Figure 2.10. The density of states around a resonance peak of frequency $\nu_0 = \omega_0/2\pi$ is given by the Lorentzian function:

$$D(\omega) = \frac{1}{2\pi}\frac{\frac{\delta\omega_0}{2}}{(\omega-\omega_0)^2 + (\frac{\delta\omega_0}{2})^2}. \tag{2.50}$$

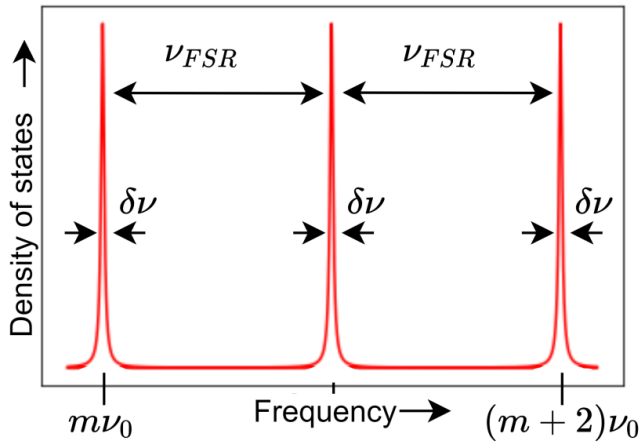

Figure 2.10: Density of states in an optical cavity. The density of states is equal to the normalized frequency spectrum of the cavity. The equidistant spacing ν_{FSR} only holds for a bare cavity, for a hybrid cavity the density of states follow the modes of Eq.(2.29). Image adapted from [30].

The spontaneous emission ratio of the NV in the ZPL is increased when the cavity and ZPL emission are on resonance, i.e. $\nu_{ZPL} = \nu_0$. The gain in emission rate achieved by altering the density of states is called the Purcell effect, which is quantified by the ratio of the emission rate in the cavity and the emission rate in free space, the Purcell factor:

$$F_P = \frac{\Gamma_{cav}}{\Gamma_{free}} = \frac{\zeta^2}{1/3}\frac{D_{cav}(\omega_0)}{D(\omega_0)} = 3\zeta^2\frac{1}{\pi^2\delta\nu}\frac{4V_0c^3}{n^3\nu^2} = \zeta^2\frac{3Q}{4\pi^2V_0}\frac{c^3}{n^3\nu^3}, \tag{2.51}$$

where $Q = (\nu/\nu_{FSR})\mathcal{F}$ is the quality factor of the cavity. Eq.(2.51) shows that the Purcell effect is optimized by maximising the finesse and minimizing the mode volume. It is important to note that the Purcell effect does not inherently change the decay channels of the NV center, but it introduces a decay channel on top of the existing ones [31]. This can be used to express the Purcell factor in terms of the lifetime of the emitter, which is defined as $\tau = 1/\Gamma_{tot}$. Consider the total decay rate of the NV center in free space and in the cavity:

$$\Gamma_{free} = \beta_0\Gamma_{free} + (1-\beta_0)\Gamma_{free}, \tag{2.52}$$
$$\Gamma_{cav} = F_P\beta_0\Gamma_{free} + \beta_0\Gamma_{free} + (1-\beta_0)\Gamma_{free}. \tag{2.53}$$

Combining Eq.(2.52) and Eq.(2.53) gives the ratio of the lifetime in the cavity and in free space:

$$\frac{\tau_{cav}}{\tau_{free}} = \frac{\Gamma_{free}}{\Gamma_{cav}} = 1 + F_P\beta_0, \tag{2.54}$$

which can be rearranged to the express the Purcell factor in terms of the lifetime in the cavity and in free space:

$$F_P = \frac{1}{\beta_0}\Big(\frac{\tau_{free}}{\tau_{cav}} - 1\Big). \tag{2.55}$$

This can be used to experimentally obtain the Purcell factor by measuring the change in the lifetime of the emitter. The overall branching ratio into the ZPL of the NV center is given by [15]:

$$\beta = \frac{\beta_0 F_P}{\beta_0 F_P + 1}. \tag{2.56}$$

3

Experimental Methods

In this chapter the experimental methods used during this thesis are discussed. Two experimental setups are utilized: a room temperature setup which is only used for the characterization of the fiber tip mirrors, and a low temperature setup for all other experiments. Since the low temperature setup is significantly more complex, this setup is discussed in greater detail. In the first section the fiber tip mirrors are discussed since these are used in both experimental setups.

3.1. Fiber Tip Mirrors

The Fabry-Pérot microcavity is composed of a concave fiber tip mirror and a macroscopic flat mirror. The dimple into the fiber tips are produced by CO_2 laser ablation, followed by the deposition of multiple layers of Ta_2O_5 ($n = 2.106$) and SiO_2 ($n = 1.488$) to create a distributed Bragg mirror coating. The amount of layers and their thickness is chosen such that light of $\lambda = 600 - 680$ nm is maximally reflected with losses of $\mathcal{L}_{fiber} \approx 50$ ppm. The flat mirror is coated with the same materials but with less layers such that $\mathcal{L}_{flat} \approx 290$. This imbalance in losses is chosen to ensure that most of the light leaves the cavity trough the flat mirror, into the collection optics. Assuming no other losses in the cavity, this gives an uppter limit to the finesse of $\mathcal{F} \approx \frac{2\pi}{340 \cdot 10^{-6}} \approx 18.000$ (Eq.(2.7)).

After machining the concave fiber tip, the profile of the fiber dimples is measured and characterized with a white light interferometer. The height profile approximates a Gaussian which is fitted to determine the radius of curvature along the two main axes, ROC_x and ROC_y, and thereby the ellipticity of the mirror. The lower part of the dimple approximates a sphere, which is fitted to determine ROC_{sphere}, further referred to as ROC. An example of the characterization of a fiber tip is shown in Appendix A.

The fibers in the room temperature setup are installed while slightly retracted from their original holders. By doing this, the fiber is clearly visible, allowing alignment by judging the reflection of the fiber in the plane mirror. Once a fiber is characterized and has favourable properties, it is transferred to a holder designed for the low temperature setup. These fibers are aligned with their reflection in a perpendicular mirror, before being retracted such that they stick out minimally with respect to the holder. The fibers are glued on the fiber holder with an epoxy glue (Stycast 2450), see Figure 3.1.

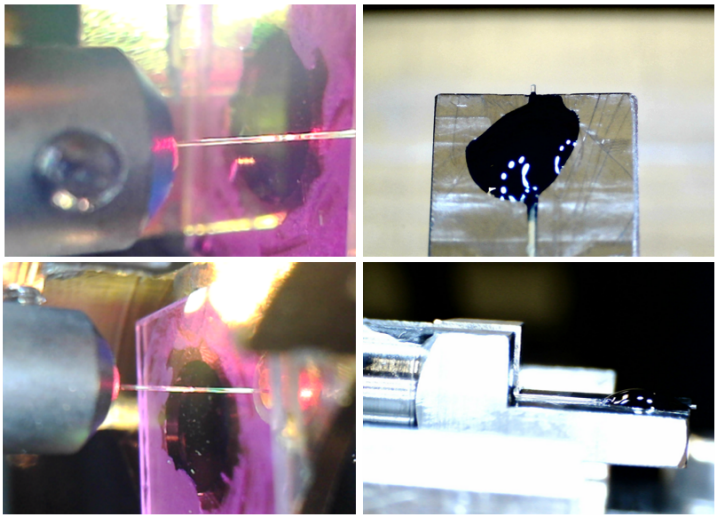

Figure 3.1: Fiber tip mirror alignment Top view (top) and side view (bottom) of fiber alignment for the room temperature setup (left) and low temperature setup (right). In the room temperature setup the fiber is retracted from its holder to allow for better angular alignment. For the low temperature setup the fiber is aligned with an opposing plane mirror (not visible) and retracted before it is glued onto the holder with epoxy.

3.2. Room Temperature Setup

A schematic view of the room temperature setup is given in Figure 3.2. The excitation setup, directly connected to the fiber has three parts: a supercontinuum white light source (filtered to $\lambda = 600 - 700$ nm, pulsed), a resonant red laser ($\lambda = 673$ nm, continuous) and an off-resonant green laser ($\lambda = 515$, continuous). The green laser is used for rough alignment since the mirrors are not reflective for this wavelength. The resonant laser input is connected to a manual polarization controller, which is fiber-coupled to the fiber tip mirror. The fiber tip mirror is secured in a holder which is mounted to both a translation and tip-tilt stage. The translation stage allows the fiber to be positioned laterally on the preferred spot on the flat mirror, and the tip-tilt stage is used for angular alignment of the fiber. In addition, this mount is equipped with a piezo which allows the fiber to be scanned and translated over a short distance in the longitudinal direction. The flat mirror is mounted on a separate translation stage opposing the fiber tip mirror, which is equipped with a piezo that allows fine translation in the lateral plane.

Two USB light microscopes are used to observe the angular alignment of the fiber tip mirror. After passing the flat mirror, the transmitted light is collected and collimated with an objective mounted on a translation stage. The objective and mirrors are used to align the beam with two pinholes to ensure that the beam is parallel to the optical table, such that the alignment remains the same after tuning the fiber angle or changing the lateral position on the plane mirror.

A 50:50 pellicle beam splitter can optionally be used to illuminate the cavity with a LED and capture an image of the fiber and plane mirror with the camera to check if there is any visible contamination. The beam is directed to a mirror on a flip mount which optionally directs the beam to photodiode to measure the transmission of the cavity. If the mirror is retracted, the beam is directed to a spectrometer to measure the frequency spectrum of the cavity.

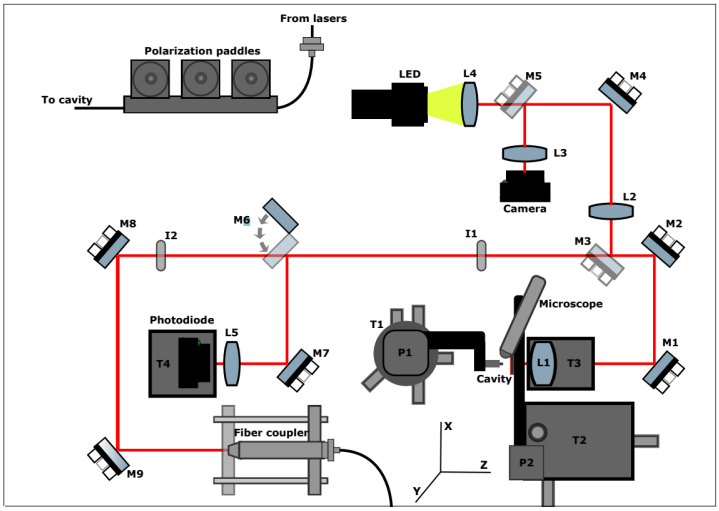

Figure 3.2: Schematic view of room temperature cavity setup. The microcavity is created by aligning a fiber tip mirror to an opposing plane mirror. The fiber is coarse aligned with a translation and tip/tilt stage (T1) and a piezo (P1) is used for fine scanning. The flat mirror is positioned with a translation stage (T2) and can be scanned laterally with piezos (P2). The cavity output beam is collected and collimated with an objective (L1) and send to either a photodiode or fiber-coupled to a spectrometer. The camera is used to inspect the mirrors for visible contamination. Image adapted from [32]

3.3. Low Temperature Setup

In this section the low temperature setup is discussed. This section is divided into different parts describing the cavity, cryostat and positioning stage. This is followed by two subsections about the optics of the setup: the excitation path and the detection path. Finally, the electronics used for the measurements are discussed. Figure 3.4 is shown to introduce some commonly used names for the parts inside the vacuum chamber.

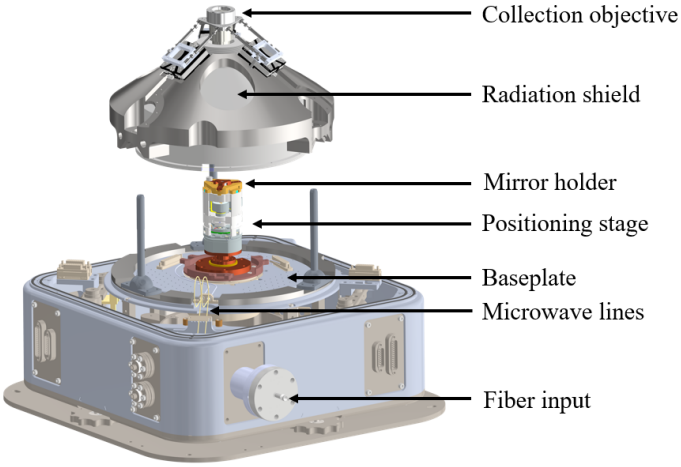

Figure 3.3: Drawing of the insert of the cryostat vacuum chamber. The cavity fiber is fed trough the fiber input and installed inside the positioning stage. The mirror holder is secured on top of the positioning stage. The lower side of the positioning stage is secured to the center of the baseplate with a vibration isolating platform. The radiation shield is used to thermally isolate the positioning stage, and the collection objective feeds the transmitted light to the detection path.

The Cavity

The cavity of the low temperature setup is used in two configurations: as a bare cavity and as a hybrid cavity containing a diamond membrane. A schematic view of both configurations is shown in Figure 3.4, and images of the configurations are shown in Appendix B.

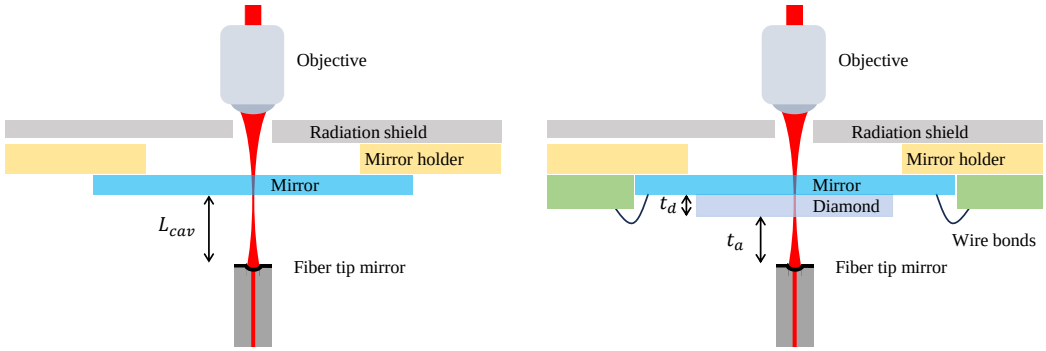

Figure 3.4: Schematic view of the microcavity configurations. The fiber tip mirror is connected to the output of the excitation path and the objective (100x magnification, 0.75 numerical aperture, 4 mm working distance, Zeiss LD EC Epiplan-Neofluar) feeds the collected transmission to the detection path. The window of the radiation shield blocks black body radiation from the room temperature objective. **Left:** Bare cavity configuration. Similar to the room temperature setup, the cavity consists of the plane mirror and fiber tip mirror separated by a distance L_{cav}. **Right:** Hybrid cavity configuration. The cavity consists of the fiber-tip mirror and plane mirror with a bonded diamond membrane. The diamond membrane has a thickness of t_d and is separated by an air gap of t_a to the fiber mirror. A support PCB is mounted on the mirror holder, and connected with wire bonds to the embedded striplines on the mirror to deliver microwaves to the diamond sample.

The bare cavity configuration is similar to the room temperature setup cavity, as it is created by moving the fiber tip close to the plane mirror. This configuration is used for the experiments in Chapter 5. In the hybrid configuration the mirror hosts a diamond sample with NV centers. The mirror is embedded with microwave striplines which are wirebonded to a PCB attached to the mirror holder, the details about the sample are discussed in section 6.1. The PCB is connected to the microwave lines with flexible microwave cables, an image is shown in Appendix C. This configuration is used for the experiments in Chapter 6.

The fiber tip mirrors are installed trough the fiber input of the vacuum chamber and connected to the excitation path, so all excitation and cavity probing happens trough the fiber tip mirror. The objective collects the transmitted light and feeds it to the detection path.

The HILA Cryostat

As previously discussed in Chapter 1, open microcavities are highly susceptible to vibrations. Operating at cryogenic temperatures is accompanied by vibrations induced by the coldhead of the cryostat, which is the main source of vibrations in the cavity. Therefore, a cryostat with a lower vibration level is chosen. The cavity is installed on a floating stage Helium-free optical closed-cycle cryostat with off-table coldhead, the Montana Instruments High Acceleration Low Inertia (HILA). The lowest operating temperature of the HILA is approximately 6 K, which is sufficient for experiments with NV centers [10]. The HILA has two advantages over other cryostats in terms of vibration isolation. First, the coldhead is isolated from the optical table where the vacuum chamber is secured. The coldhead is only connected to the vacuum chamber with a flexible vacuum bellow and loose thermal braids. This minimizes the transfer of vibrations from the cold head to the optical table, and thereby to the cavity. Second, the baseplate inside the vacuum chamber is isolated from the optical table using electromagnets with an automatic levelling system. The baseplate is equipped with a large mass, thereby acting as a mechanical short-pass filter with cutoff frequency ~ 1 Hz.

The Positioning stage

The positioning stage that hosts the cavity is the Cryo Positioning Stage High Resonance (CPSHR1-a) from Janssen Precision Engineering (JPE). A schematic of the stage is shown in Figure 3.5.

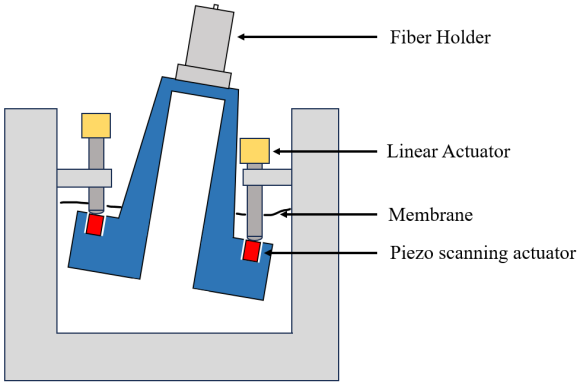

Figure 3.5: Schematic view of positioning stage. The fiber holder is secured to a tripod system (blue). The tripod is held under tension with a membrane (black) that pushes it upwards, while three linear actuators (yellow) push it down. This allows the fiber holder to be moved in three dimensions by moving the linear actuators up and down. The cavity length is scanned by applying an AC voltage to the scanning actuators (red) embedded between the contact points of the linear actuators and the tripod.

The positioning stage is equipped with three linear actuators that are attached to a tripod system that holds the fiber holder. The fiber holder can be moved in all directions by moving the linear actuators up and down. In addition, piezo scanning actuators for fine control are embedded between the contact points of the linear actuators and the tripod system. This allows fast scanning of the cavity length by applying an AC voltage to these actuators.

The positioning stage has a mechanical resonance frequency of ~ 3800 Hz without load and is secured to the baseplate on an additional vibration isolation platform (JPE CVIP1). This platform acts as a mechanical short-pass filter with a cutoff frequency of 42 Hz. The mismatch in resonance frequency between the vibration isolation platform and the positioning system is advantageous for reducing the vibrations in the cavity further, since the vibrations that excite the high resonance frequency of the positioning stage are attenuated by the isolation platform.

3.3.1. Excitation Path

In this section the excitation path of the low temperature setup is discussed. In the excitation path the following five light sources are used:

- Toptica DLC Pro ($\lambda = 637$ nm, continuous. fiber-coupled); referred to as resonant laser 1
- New Focus Velocity TLB-6300-LN (637 nm, continuous, fiber-coupled); referred to as resonant laser 2
- Hübner Photonics Cobolt MLD 515 ($\lambda = 515$ nm, continuous, fiber-coupled); referred to as off-resonant green laser
- NKT Photonics Katana-05HP ($\lambda = 532$ nm, pulsed, 230 ps pulse duration, 5-12 MHz repetition rate , free space); referred to as off-resonant pulsed green laser
- NKT Photonics SC-450-2 ($450 - 2000$ nm, pulsed, fiber-coupled); referred to as supercontinuum white light source

The excitation path is composed of three sections: the red laser path, the green laser path and the white light source path. The red and green lasers paths are coupled into the same input of a 4×1 single mode fiber switch box (Agiltron custom version) and the white light is coupled into a separate input of the fiber switch box. A schematic of the excitation path is given in Figure 3.6.

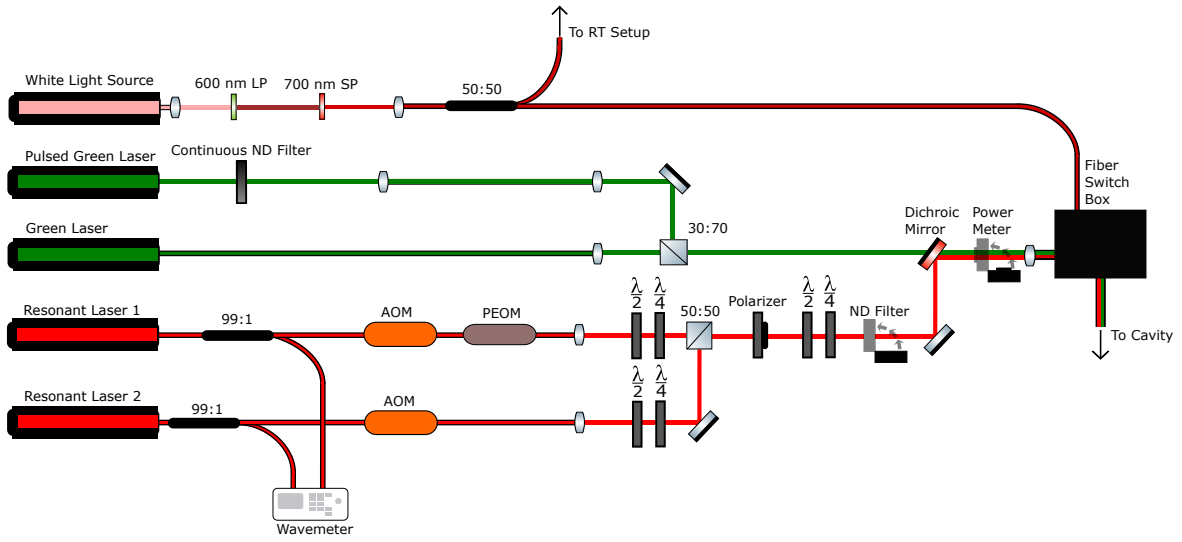

Figure 3.6: Schematic view of excitation path. Fibers are indicated with black edges around the beams. Lenses indicate objectives/collimators that couple to free space. The excitation path consists of the red laser path, the green laser path and the white light source path. The red and green laser paths are combined on a dichroic mirror and collected in the same input of the fiber switch box. The white light source is filtered to $\lambda = 600$-700 nm and collected in a separate input of the fiber switch box.

The emission of the white light source is collimated into free space and filtered with a 600 nm long-pass filter and 700 nm short-pass filter, after which it is collected in a single-mode fiber with an objective. The single mode fiber is connected to a 50:50 fiber beam splitter with one output guided to the room temperature setup and the other output connected to the fiber switch box.

The red laser path is followed by resonant laser 1 and 2. The emission of the lasers is partially directed to a wavemeter (HighFinesse WS-U) with 99:1 fiber beamsplitters to monitor the wavelength of the emission, which enables the lasers to be frequency-stabilized. The output of both lasers is guided through an acoustic-optic modulator (AOM) (Gooch and Housego Fiber-Q 633 nm) which are used to calibrate and attenuate the laser power. Additionally, resonant laser 1 is connected to a phase electro-optic modulator (PEOM) (Jenoptik PM635, driven by a Rohde and Schwarz SGS100A signal generator), which allows sideband modulation (further discussed in Section 4.1). Both lasers are collimated into free space with an objective and guided trough a half-wave plate (HWP) and quarter-wave plate (QWP) for individual polarization control, before being combined with a 50:50 beamsplitter. The combined beam is sent though a linear polarizer and a HWP and QWP for polarization control. A retractable neutral density filter is placed after the polarization optics. This is used to heavily attenuate the laser power when using the avalanche photo diodes (APDs) (Laser Components COUNT-10C-FC). The beam passes the dichroic mirror (Semrock FF560-FDi01) that combines the red and green laser path before it is coupled into the input of the fiber switch box.

The emission of the pulsed green laser is passed trough a continuous neutral density filter which can be rotated to attenuate the laser power to a desired value. The emission of the green lasers is combined with a 30:70 (pulsed:continuous) beam splitter and reflected of the dichroic mirror, thereby combining the red laser path and green laser path emission. A retractable power meter is placed in front of the input of the fiber switch box to measure and calibrate the power of the lasers of both paths.

3.3.2. Detection Path

In this section the detection path of the low temperature setup is discussed. The detection path is composed of four sections: the spectrometer path, the photodiode path, the ZPL path and the PSB path. A schematic of the detection path is given in Figure 3.7.

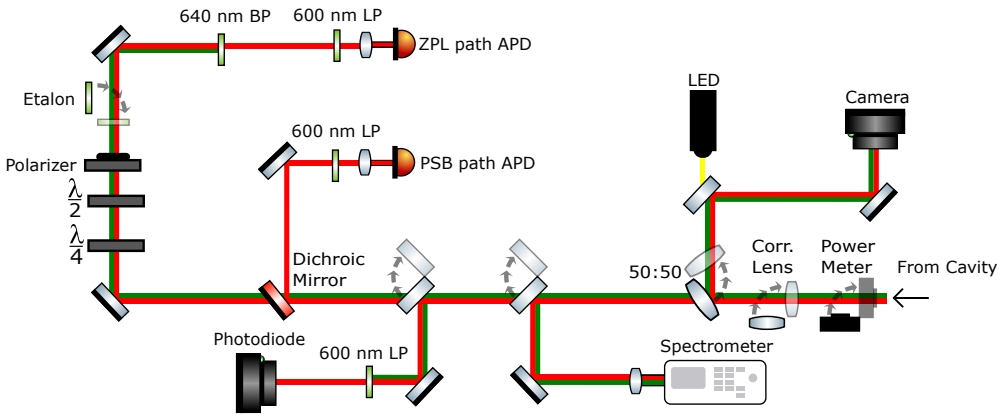

Figure 3.7: Schematic of detection path. The detection path consists of the spectrometer path, the photodiode path, the ZPL path and the PSB path. The cavity can be imaged with a retractable 50:50 pellicle beam splitter and corrective lens. Two retractable mirrors can be used to guide the beam to the spectrometer path or photodiode path. The PSB and ZPL path are split with a dichroic mirror.

A retractable powermeter is placed at the beginning of the detection path to measure the power of the light coming from the cavity. A 50:50 pellicle beam splitter (Thorlabs BP150) and a corrective lens are positioned on flip mounts, directing the beam path towards a camera and LED to image the fiber tip and diamond sample. Two retractable mirrors are placed in the beam path that can direct the beam to the spectrometer path or the photodiode path. In the spectrometer path the beam is coupled in to a single mode fiber which is connected to the input of the spectrometer (Princeton Instruments SP-2500i with coarse grating 300 g/mm, fine grating 1800 g/mm). In the photodiode path the light is filtered with a 600 nm long-pass filter (Thorlabs FESH0600) before it is detected with the free space photodiode (Thorlabs APD 130A2/M). If the two mirrors are both retracted, the beam is split on a dichroic mirror (Semrock DI 02-P365) to the PSB path and ZPL path. The PSB path is filtered with a 645 nm long-pass filter (Semrock BLP01-633R-25) and coupled into a fiber connected to an APD. The ZPL path contains a HWP, QWP and a retractable linear polarizer, which can be used for polarization control and filtering resonant excitation laser light from ZPL emission (further discussed in Section 5.2). After the polarization optics, a retractable etalon (LightMachinery custom coating) with FWHM $\approx$ 100 GHz is placed on a rotation mount to filter the ZPL light. The etalon can be rotated to tune the transmission frequency. The light is additionally filtered with a 640 nm band-pass filter (Thorlabs FBH640-10, FWHM = 10 nm) and a 600 nm long-pass filter (Thorlabs FESH0600), before it is collected and sent to the APD.

3.3.3. Electronics

The measurements are coordinated by a real-time microcontroller (Jäger ADwin PRO II), which is equipped with analog and digital in- and outputs, as well as a counting module for the APDs. The ADwin has a time resolution of $\sim$ 1 µs. For experiments that require better time resolution, such as the lifetime measurements in Section 6.3, a single photon counting module (Picoquant HydraHarp 400) is used as timetagger. The free space photodiode is connected to two oscilloscopes, the Picoscope 3403D MSO and the Yokogawa DLM5000 Series Mixed Signal Oscilloscope. The Yokogawa has a time resolution of 800 ns and can record up to 250 million data points, which is needed for the vibration measurements in Section 5.1. The microwave driving of the NV centers in Section 6.4 is conducted with a vector signal generator (Rohde & Schwarz SMBV100A).

4

Fiber Mirror Characterization

In this chapter the characterization of the fiber tip mirrors is discussed. The performance of the fiber tip mirrors is quantified by measuring the maximally obtainable finesse. In the first section the methods of measuring the finesse is presented, followed by a section containing the results of the measurements. All fiber tip mirrors are characterized in the room temperature setup.

4.1. Methods for Fiber Mirror Characterization

As discussed in Section 2.2.1, the finesse can be determined experimentally by measuring the linewidth and Free Spectral Range (FSR) of the cavity. While the FSR can be obtained from a spectrometer measurement, the resolution of the spectrometer is not accurate enough to resolve the linewidth of the cavity. Therefore, the cavity linewidth is measured with a photodiode while scanning the cavity length. In this section multiple measurement methods are discussed, including cavity length measurements, sideband modulation and two laser linewidth scanning for linewidth measurements, and fundamental mode scanning for directly measuring the finesse.

Cavity length measurements

For cavity length measurements the cavity is probed with the white light source (filtered for $\lambda = 600-700$ nm) and the transmitted light is sent to the spectrometer. The measured spectrum contains peaks of transmission, separated by the FSR of the cavity. The obtained FSR of the cavity is used to calculate the cavity length according to Eq.(2.9). Two examples of obtained spectra at different cavity lengths are shown in Figure 4.1.

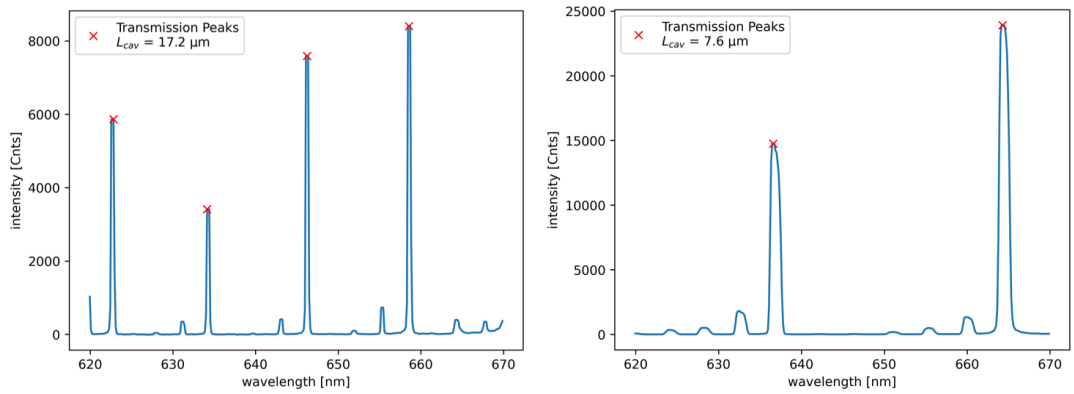

Figure 4.1: Spectra of cavity length measurements. The fundamental modes are indicated with red crosses. The FSR is calculated by taking the average frequency between subsequent fundamental peaks.

Although the cavity length measurement seems straightforward, with some fiber tip mirrors the higher

order modes are prominent which makes the distinction between fundamental and higher order modes difficult. This effect can be minimized by alignment of the beam path and by using pinholes to partially cut off the beam, since the intensity profile of higher order modes are spread out more in the lateral plane.

Linewidth measurement by sideband modulation

To obtain the linewidth, the cavity is probed with resonant laser 1 and the transmission is measured with the photodiode. Resonant laser 1 is fiber-coupled with a phase electro-optic modulator (PEOM), which generates sidebands with a detuning of $\leq \pm 9$ GHz. The transmission is measured while scanning the cavity length over a small distance around the resonance peak. The sideband detuning is used to calculate a conversion factor between time and frequency, which is used to calculate $\delta\nu$. The relation between time and cavity length is assumed to be linear. An example of a transmission plot with and without sideband modulation is given in Figure 4.2.

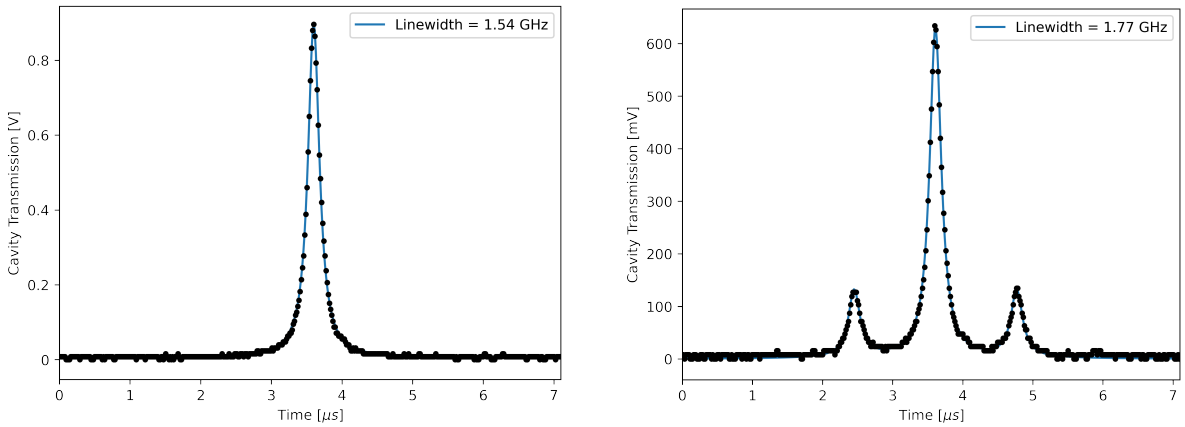

Figure 4.2: Sideband modulation linewidth measurement. The cavity length is scanned at 3000 Hz while probing with resonant laser 1. **Left**: The transmission of the cavity without sideband modulation. **Right**: Transmission of the cavity with sideband modulation. The sidebands have a detuning of ± 9 GHz with respect to the resonance peak. With this detuning, the time axis is converted to a frequency axis to calculate the linewidth of the cavity.

Linewidth measurement with two resonant lasers

Similar to sideband modulation, this method is used to measure the linewidth of the cavity with the photodiode. Two frequency-stabilized resonant lasers are needed for this method, so this is only used on the low temperature setup. The frequency of the two laser are set a few tens of GHz apart. The transmission is measured while scanning the cavity length for a distance long enough to show the transmission peaks of both lasers. The precise laser frequency is measured by a wavemeter, and used to calculate a conversion factor between time and frequency, from which $\delta\nu$ can be calculated for both peaks. An example of a two laser linewidth scanning transmission plot is given in Figure 4.3.

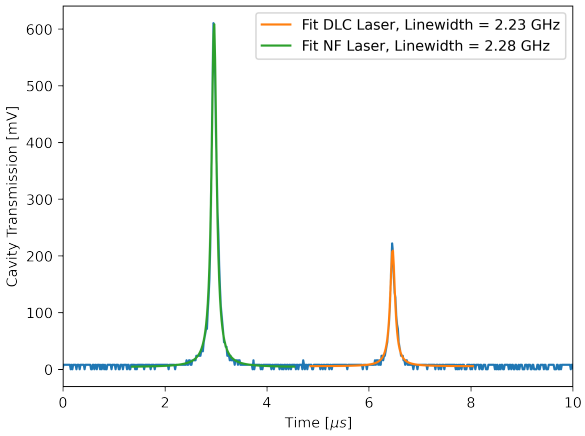

Figure 4.3: Two laser linewidth measurement. The cavity length is scanned at 3000 Hz while probing with the frequency-stabilized resonant lasers 1 and 2. The known laser frequencies are used to calculate a conversion factor between time and frequency which is used to calculate the linewidth.

Finesse measurement by scanning fundamental modes

For this method only the photodiode is used. The cavity is probed with one of the resonant lasers while the cavity length is scanned over a length larger than $\lambda/2$. Since the resonance condition for a bare cavity is periodic with $\lambda/2$, the transmission of one scan contains two fundamental modes of the cavity. An example is shown in Figure 4.4.

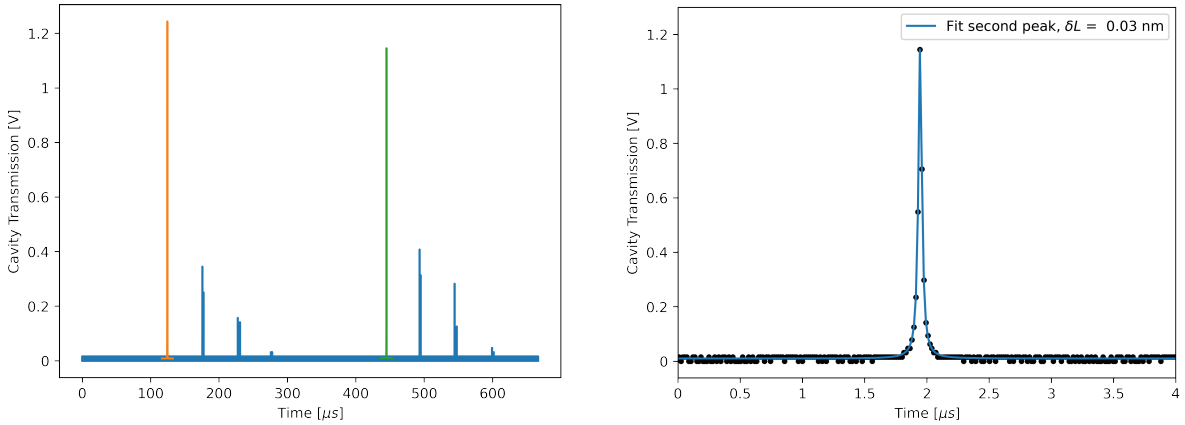

Figure 4.4: Transmission of fundamental mode scan. The cavity length is scanned at 300 Hz for a length larger than $\lambda/2$. **Left**: The two fundamental peaks (highlighted) are clearly visible as well as some higher order modes. The frequency splitting of the higher order modes is due to the ellipticity of the fiber dimple. **Right**: Zoomed in graph of the second resonance peak. The peak is fitted with a Lorentzian function to determine the FWHM of the peak and converted to δL_{cav} with a time to length conversion factor.

The time axis can be converted to a length axis, since the time difference of the two fundamental peaks corresponds to a cavity length change of $\lambda/2$. This reveals the spatial linewidth δL_{cav}, which can be converted to the cavity linewidth $\delta\nu$. Starting from the resonance condition (Eq. (2.8)):

$$\nu_m(L_{cav}) = m\frac{c}{2nL_{cav}}.$$

Assuming the deviation in cavity length over the width of the resonance peak is small, the linear approximation is used to find the cavity linewidth:

$$\delta\nu = \left|\frac{\partial\nu_m}{\partial L_{cav}}\right| \delta L_{cav} = \frac{mc}{2nL_{cav}^2}\delta L_{cav}. \tag{4.1}$$

Combining this with Eq.(2.12) and using $L_{cav} = m\lambda/2$, the finesse can be expressed as:

$$\mathcal{F} = \frac{\nu_{FSR}}{\delta\nu} = \frac{c/2nL_{cav}}{mc/2nL_{cav}^2}\frac{1}{\delta L_{cav}} = \frac{L_{cav}/m}{\delta L_{cav}} = \frac{\lambda/2}{\delta L_{cav}}. \tag{4.2}$$

From experience it seems that the non-linearity of the scanning piezo induces a small linewidth broadening of the transmission spectrum, which becomes more severe at higher scanning amplitudes. This is in agreement with the results of [32]. Since the sideband modulation method requires a far lower scanning amplitude, this effect is negligible for this method, which makes the approximate linear correlation between time and cavity length more accurate. However, since experimentally the fundamental mode scanning method is significantly faster, this method is chosen to characterize the fiber tip mirrors. This choice is made because the relative performance between the fiber tip mirrors is more important than the absolute value of the obtained finesse.

4.2. Results of Fiber Mirror Characterization

Thirteen fiber tip mirrors are characterized with the fundamental mode scanning method. The finesse is measured in a range of cavity lengths for each mirror. The maximum obtainable finesse is used to quantify the performance of the mirror. The results are shown in Figure 4.5.

From the results it is apparent that the finesse can vary significantly for repeated measurements, for all the measurement methods discussed in the previous section. This fluctuating in finesse is common in literature, see for example [27], [33]. The obtained error from fitting the plots is significantly smaller than the variation of the obtained finesse values. Therefore, the error of the finesse is estimated with multiple measurements for different values and cavity lengths, which results in $\sim \pm 5\%$. This is in line with the variations found in literature.

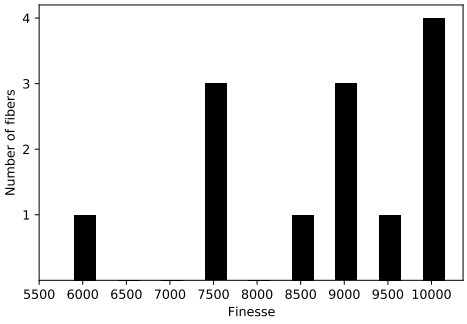

Figure 4.5: Histogram showing the maximum obtained finesse for each fiber. Thirteen fiber tip mirrors are characterized with the fundamental mode scanning method. Three fibers obtained a finesse of $\mathcal{F} > 9500$. The histogram has bin size 500.

Four of the thirteen characterized fiber tip mirrors achieved a finesse of $\mathcal{F} > 9500$. The maximum measured finesse of the mirrors is ~ 8000 lower than the mirror coating limit. This means that there are unaccounted losses of $\mathcal{L}_{ext} \approx 280$ ppm. It is unclear where these losses originate from, but some possible sources are the imperfectness of the dimple shape and the surface roughness of the mirrors. To understand the origin of the differences in obtained finesse values of the fibers, the maximum finesse is plotted against the *ROC* and the asymmetry of the dimples, shown in Figure 4.6.

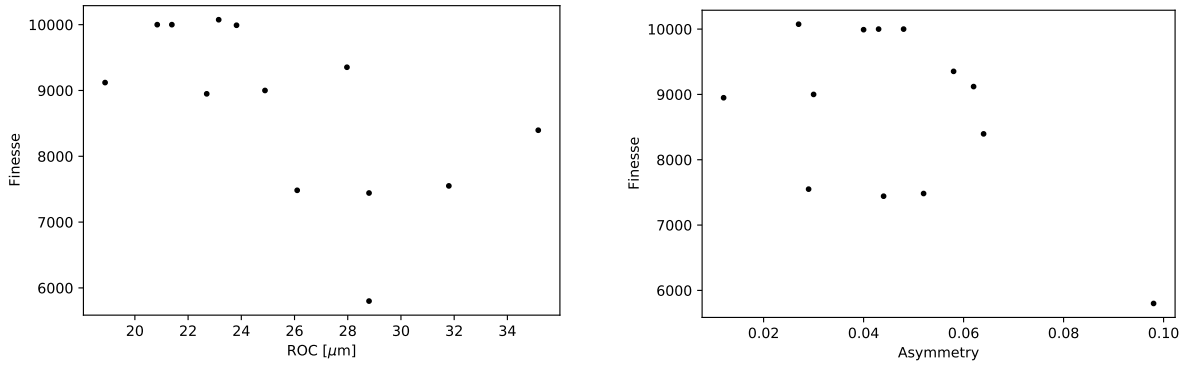

Figure 4.6: Finesse statistics for dimple parameters. The maximum obtained finesse is plotted against the *ROC* (left) and asymmetry (right) of the dimple. The plots show no clear correlation between finesse and *ROC* or asymmetry.

The plots in Figure 4.6 show no clear correlation between finesse and *ROC* or asymmetry of the fiber dimple. However, there is an indication that a smaller *ROC* is better for cavity performance. In addition, the finesse seems to drop for the data point at asymmetry ≈ 0.10. While the single data point does not show a correlation, a drop in finesse is expected as the Gaussian wavefront matches the dimple the best when the asymmetry is minimal.

Several properties of the fiber tip mirrors where found during the measurements. The most important property is that the performance of the mirror is highly dependent on the angular alignment between the fiber and the plane mirror, an example is shown in Figure 4.7.

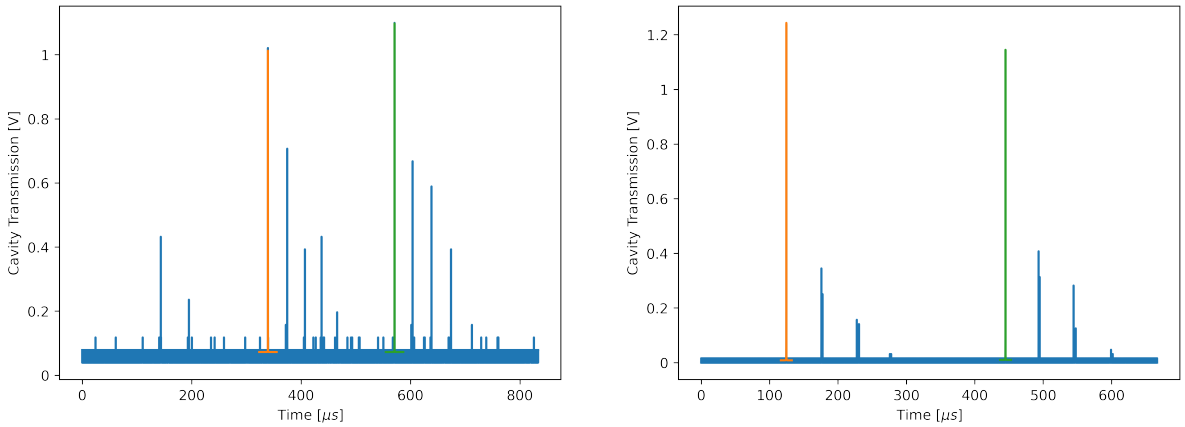

Figure 4.7: Effect of angular alignment on cavity performance. Resonance peaks of fundamental modes are highlighted. **Left**: Transmission scan with a fiber aligned with one USB light microscope ($\mathcal{F} \approx 6300$). **Right**: Transmission scan with a fiber aligned with two perpendicular USB light microscopes ($\mathcal{F} \approx 9000$). The misaligned cavity has a significantly lower finesse and the higher order modes are much more prominent, which make cavity length measurements difficult.

Angular misalignment increases the prominence of the higher order modes and decreases the achievable finesse. Due to these results, the alignment method for the low temperature setup was also changed to include two perpendicular USB light microscopes instead of one, as previously discussed in Section 3.1.

The best performing fiber is chosen to be used in the low temperature setup. The finesse measurement and two length measurements of this fiber are shown in Figure 4.8 and 4.9.

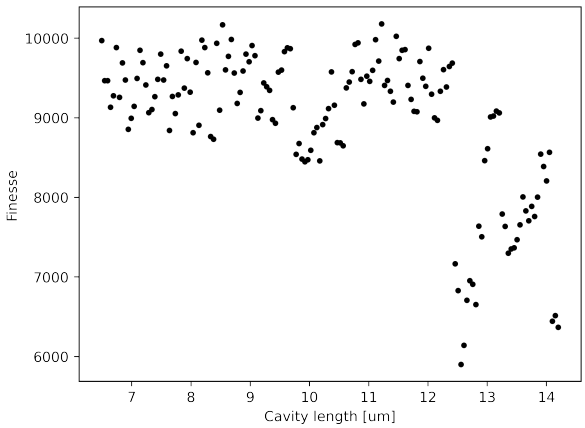

Figure 4.8: Finesse measurement of the best performing fiber. The finesse is measured for for cavity lengths between 6.5 µm and 14.5 µm. The finesse is stable at $\mathcal{F} \approx 9500$ before it drops after a cavity length of 12 µm due to clipping losses.

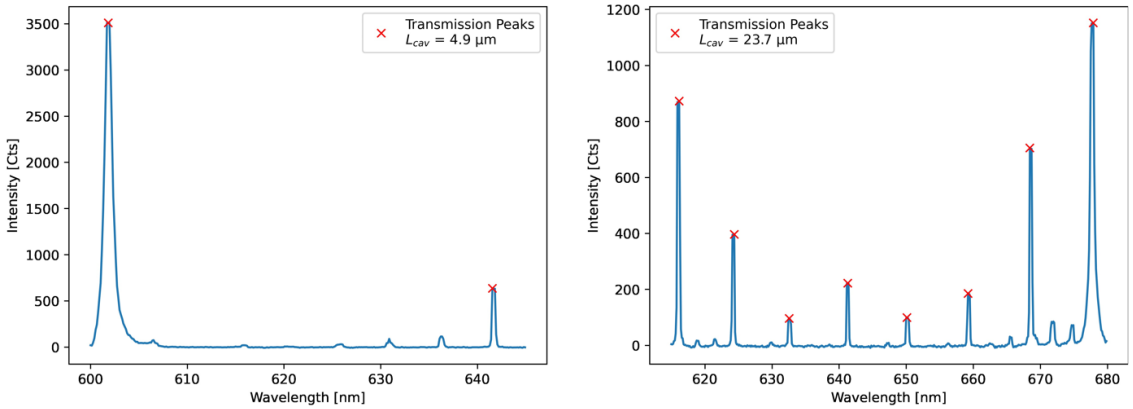

Figure 4.9: Length measurements of the best performing fiber. Length measurements are done for a short cavity (left) and long cavity (right), resulting in cavity lengths of (4.9 ± 0.1) µm and (23.7 ± 0.05) µm respectively. The spectra show very few higher order modes.

The Figure 4.8 shows that the fiber obtains a stable finesse of $\mathcal{F} \approx 9500$ for a long range in cavity length, and Figure 4.9 shows that the cavity has a clean white light spectrum with few higher order modes. This fiber is used for the remainder of the experiments in this thesis.

5

Bare Cavity Characterization

In this chapter characterization of the bare cavity is discussed. In the first section the methods and results of the vibration measurements are shown. In the second section the preparation for further measurements is discussed. This includes measurements that are necessary for further experiments with NV centers that are outside the scope of this thesis, such as resonant laser scans, polarization suppression and collection efficiency measurements.

5.1. Vibration Measurements

The tunability of open Fabry-Pérot microcavities is accompanied with a high susceptibility to vibrations. As previously discussed in Chapter 1, these vibrations lead to cavity length fluctuations, which result in fluctuations of the resonance frequency. Therefore, it is important to quantify the amplitude and frequencies of the vibrations to be able to identify their origin and mitigate them. The methods of measuring vibrations and their results are discussed in this section.

5.1.1. Methods of Measuring Vibrations

The vibrations of the bare cavity are measured by analyzing the transmission of the cavity. To measure the vibrations, the cavity parameters L_{cav}, $\delta\nu$ and maximum transmission voltage V_{max} have to be known. The cavity length is set such that it is slightly off-resonance, resulting in a measured transmission voltage $V_{trans} < V_{max}$. The linewidth $\delta\nu$ and V_{max} fully define the Lorentzian profile of the cavity transmission voltage. This allows the measurement of the detuning in cavity resonance frequency $\Delta\nu$ by checking at what detuning the voltage V_{trans} is reached. This change in resonance frequency is converted to a change in cavity length using [34]:

$$\frac{\Delta\nu}{\nu} = \frac{\Delta L}{L} \quad \rightarrow \quad \Delta L_{cav} = \frac{\Delta\nu}{\nu} L_{cav}. \tag{5.1}$$

To prepare the measurement, the cavity linewidth is measured with the two-laser linewidth scanning method and the cavity length is measured with the white light source (See Section 4.1). Next, the maximum transmission voltage of the cavity is measured, followed by acquiring a time trace of the transmission voltage of ten seconds measured with an oscilloscope (Yokogawa DLM5000 Series Mixed Signal Oscilloscope). The Yokogawa is used because it has a high time resolution, set to 800 ns, allowing vibration measurements of up to $f = 625$ kHz, which is well above the expected range from mechanical vibrations in the cavity.

The measured transmission voltage trace is converted to a change in cavity length. This curve is detrented to counteract any change in transmission voltage due to cavity length drifts and reveal the absolute length detuning. An example is shown in Figure 5.1.

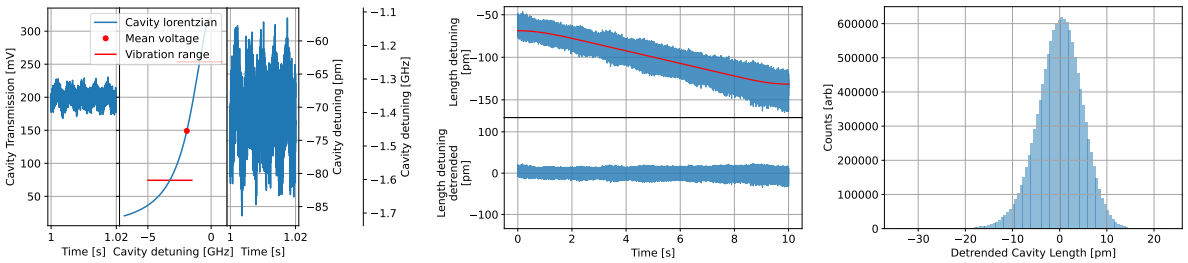

Figure 5.1: Vibration measurements methods. Data is taken at room temperature while the coldhead is turned off. **Left:** The transmission voltage is converted to a resonance frequency detuning by checking for what frequency detuning the the measured voltage is reached on the cavity Lorentzian. This frequency detuning is converted to a length detuning with Eq.(5.1). **Middle:** The cavity detuning curve is detrented to counteract any change in voltage due to cavity length drifts and reveal the absolute length detuning. The curve used for detrenting is shown in red. **Right:** Histogram of the detrented cavity length detunings. The measured vibrations follow a Gaussian distribution.

The histogram of the detuned cavity length in Figure 5.1 shows that the vibrations in the cavity follow a Gaussian distribution, which is expected from the literature [31]. Therefore, the effects of the vibrations on the achievable Purcell factor are modelled with vibrations that follow a Gaussian distribution, this is further discussed in Section 6.1.
Finally, the length detuning trace is analyzed by computing the RMS value of the vibrations and taking the Fast Fourier transform (FFT) to identify the frequencies of the vibrations. An example of this is shown in Figure 5.2.

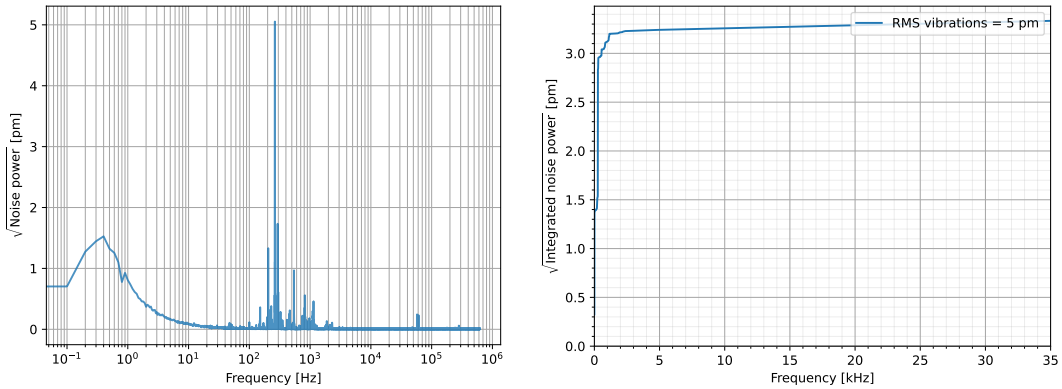

Figure 5.2: Example of vibration measurement analysis. Results of the same dataset used in Figure 5.1. **Left:** The FFT of the length detuning trace is taken to reveal the frequencies of the vibrations in the cavity. The frequency axis is plotted in logarithmic scale. **Right:** Cumulative FFT of the length detuning trace. This plot shows the same information as the plot on the left, but is often preferred to see the contributions of the vibrations in the 1-5 kHz range more clearly.

Before doing the vibration measurements, the following points need to be considered. First, it is important that the measured transmission voltage does not reach V_{max}. If this happens, it is most likely that the transmission is measured on the other side of the peak of the cavity Lorentzian, which means that the cavity detuning is underestimated. In addition to not setting the initial V_{trans} too high, this overshooting of transmission voltage can be avoided by measuring the vibrations in a cavity with low finesse. To see why, consider the length change needed to detune a cavity by its linewidth: $\Delta L_{cav} = \frac{\delta\nu}{\nu} L_{cav} = \frac{\lambda}{2\mathcal{F}}$. The length detuning needed to detune the cavity by its linewidth increases by lowering the finesse, which decreases the chance of detuning the cavity such that the transmission is measured on the wrong side of the cavity Lorentzian. In addition, a lower finesse equals to a broader linewidth which has a less steep relation between transmission voltage and frequency detuning than a sharp linewidth, thereby increasing the resolution in frequency. For these reasons the cavity vibrations are measured with long cavity lengths, such that the finesse is decreased due to clipping losses.

5.1.2. Results of Vibration Measurements

The vibrations of the bare cave are measured for a cavity with $L_{cav} = (23.4 \pm 0.05)$ µm and $\delta\nu = (1.75 \pm 0.03)$ GHz, resulting in a finesse of $\mathcal{F} \approx 3700$. Since the coldhead of the cryostat is the dominant source of the vibrations, the vibrations are analyzed for both high (C: 30 Hz, 70 Hz) and low (C: 14 Hz, H: 40 Hz) coldhead cycle frequency settings. The vibrations are measured at $T \sim 7.5$ K. The transmission of resonant laser 1 is measured for 10 seconds on the Yokogawa oscilloscope and converted to a length detuning trace, the results are shown in Figure 5.3.

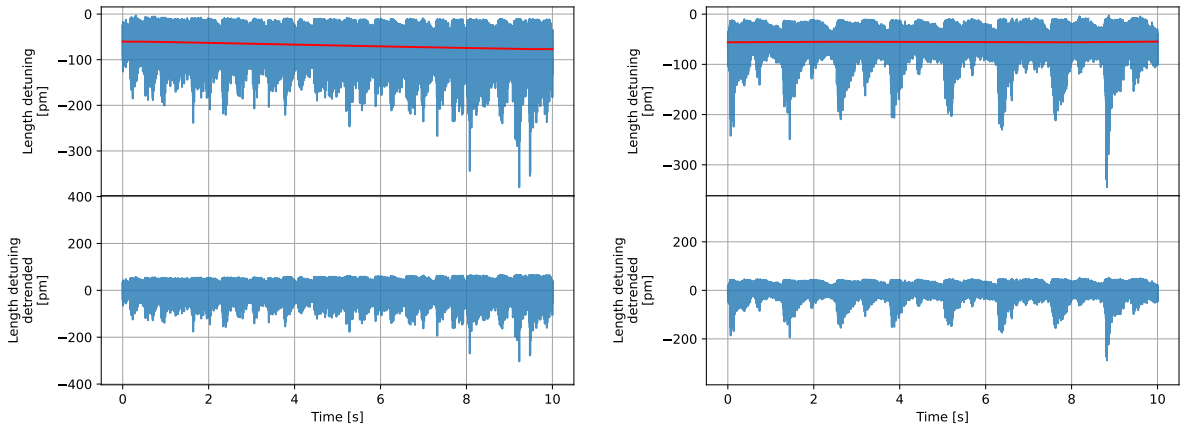

Figure 5.3: Cavity length detuning traces. Data is taken at $T \sim 7.5$ K for high (left) and low (right) coldhead cycle frequency settings. The length detuning is measured for 10 seconds. The detrending curve is shown in red. The cycle frequency of the different coldhead settings are visible in the detuning.

The effect of the different coldhead cycle frequencies is visible in the frequency of large detuning peaks in the time traces. The times where the coldhead mechanically excites the systems are clearly visible for the low settings, which are followed by a time that the vibrations relax. The periodicity of this trend can be utilized to only measure at times where the vibrations are more quiet to decrease their effect on the experiment [31]. For the high coldhead settings this is not possible, as the system is mechanically excited again before the vibrations relax.

The length detuning traces are analyzed by taking the FFT, see Figure 5.4. The FFT spectra show that the majority of the vibrations are at $f = 2$ kHz and $f = 4$ kHz. These are attributed to resonance frequency of the positioning stage, shifted from the load of the fiber holder (see Section 3.3). The obtained RMS values of the cavity length detuning are $\sigma_{vib,high} = 22$ pm and $\sigma_{vib,low} = 18$ pm, concluding that the performance of the passive stabilization of the bare cavity is excellent. The high coldhead cycle frequency settings are used for the remainder of this thesis, since the thermal stability is better for these settings while the added vibrations are minimal.

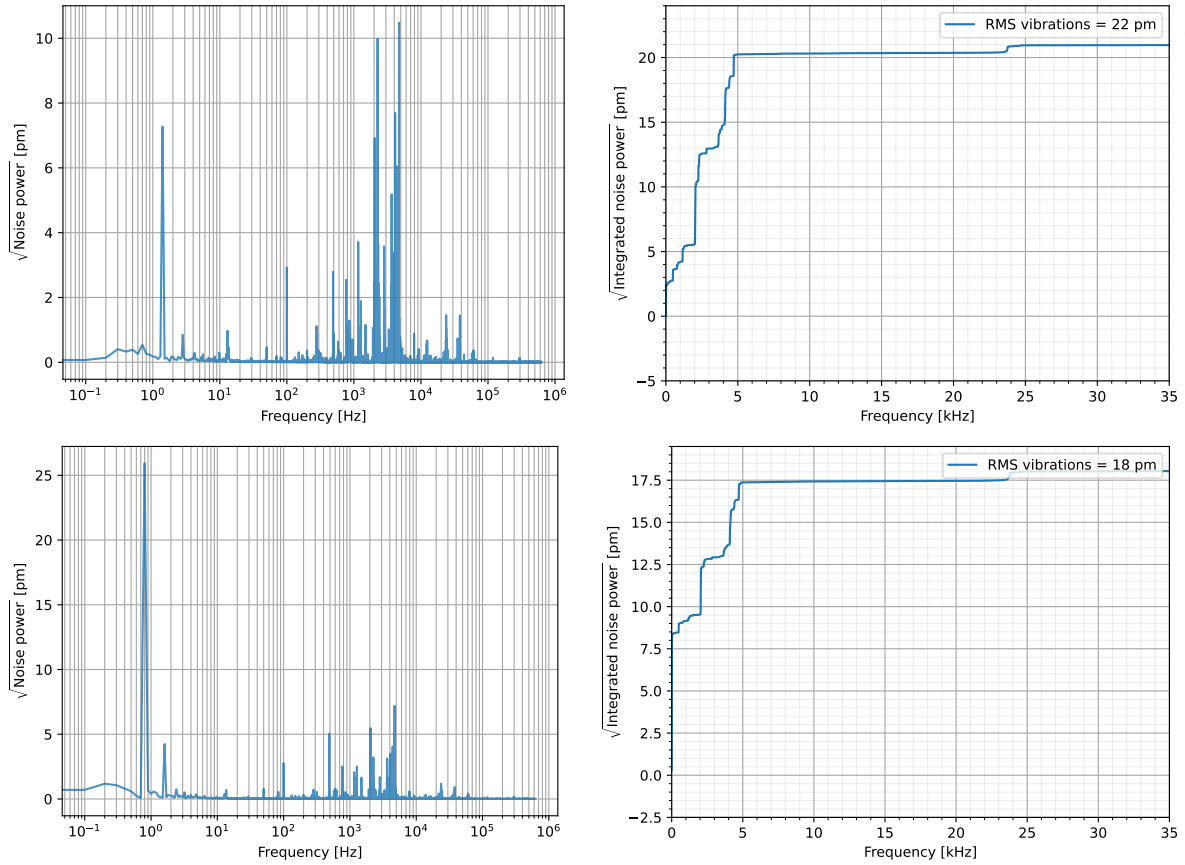

Figure 5.4: Results of vibration measurements Data is taken at $T \sim 7.5$ K for high (top) and low (bottom) coldhead cycle frequency settings. The FFT (left) and cumulative FFT (right) of the length detuning traces show that the majority of the vibrations are at $f = 2$ kHz and $f = 4$ kHz.

5.2. Preparation for Further Measurements

In this section some measurements are discussed which are necessary for further experiments with NV centers that are outside the scope of this thesis. This includes resonant laser scans, polarization suppression and collection efficiency measurements.

Resonant laser scans

In the experiments with the NV centers in Chapter 6 the NV centers are off-resonantly excited with green laser light. For future measurements it is necessary to resonantly excite the NV centers as this is needed for spin readout, state initialization and spin-photon entanglement [10]. For these implementations, the NV is driven at certain transitions, which frequencies are determined in photoluminescence excitation (PLE) measurements. This is accomplished by sweeping the resonant laser frequency over the resonance frequencies of the individual transitions while collecting the emission of the NV center. In addition to PLE measurements, scanning the frequency of the excitation laser is used in other measurements, such as showing non-linear behavior of an emitter-cavity system with a transmission dip measurement [35]. While these measurements are outside of the scope of this thesis, some resonant laser scan measurements are measured as proof of principle demonstrations for the current setup configuration. An example is shown in Figure 5.5.

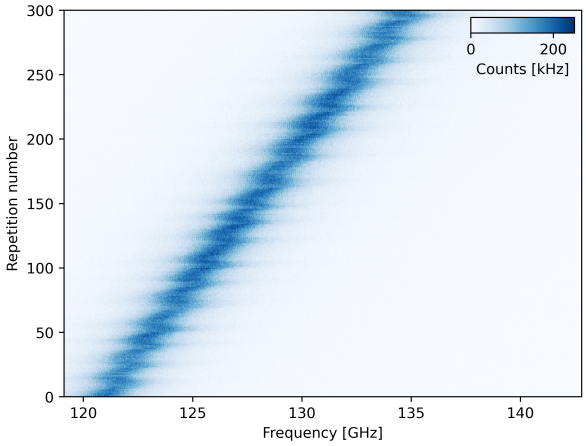

Figure 5.5: Resonant laser scan. Frequency axis is w.r.t. 470.4 THz. Resonant laser 1 is attenuated and scanned from 120 to 145 GHz while collecting in the ZPL path. For each repetition the cavity length slightly drifts, resulting in an increase in resonance frequency of the cavity.

Polarization suppression

Resonant excitation comes with the downside that the excitation light can no longer be filtered from the ZPL emission with a spectral filter. Efficient filtering of the laser light is important for quantum information applications, since measured events due to leaking laser light would result in incorrectly heralded entanglement, thereby reducing the state fidelity. To distinguish between ZPL photons and laser light, a cross-polarization scheme is used. The polarization of the laser light is set to an angle with the polarization of the ZPL emission, which allows the filtering of the laser light by setting a polarizer perpendicular to the polarization of the laser.

The suppression of the laser light is tested with a linear polarizer and half-wave plate (HWP) in detection. The HWP is initialized in the angle corresponding to maximum suppression. It is then rotated between 0 and 180 degrees in thirteen steps. For each measurement resonant laser 1 is used to do fifteen fast laser scans. The results are shown in Figure 5.6.

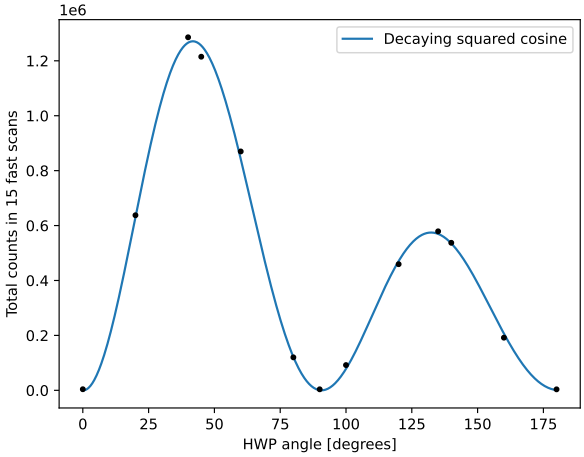

Figure 5.6: Polarization suppression measurement. Each data point contains the integrated counts of 15 resonant laser scans. The laser scans are done by scanning the resonant laser with a power of ~ 2 nW over a range of 25 GHz in 2 seconds while collecting in the ZPL path. The decaying squared cosine is added as a guide to the eye. The decaying nature of the data originates from a small misalignment during the measurement due to cavity length drifting.

The decaying nature of the data originates from a small misalignment during the measurement due to cavity length drifting. After the measurement the same maximum count rate was achieved by realigning the setup. The obtained count rate for no suppression is 650 kHz, and for maximum suppression 550 Hz, resulting in a maximum suppression of ~ 30 dB. This is comparable to spin-photon entanglement experiments found in literature, where time filtering in combination with polarization suppression is used [36].

Collection efficiency

As previously discussed in Chapter 1, the maximally achievable entanglement rate is suppressed by the product of all losses in the system. One significant loss in the system originates from the collection of photons into the single mode fiber. It is necessary to use a single mode fiber to reduce the collection of background photons, but obtaining a high collection efficiency is challenging due to the small area of the core of the fiber. The collection efficiency is measured for five different lenses/objectives, the results are shown in Table 5.1.

Table 5.1: Collection Efficiencies for different setup configurations. The collection efficiency is measured as the ratio between the intensity before the collection lens/objective and the intensity after the single mode fiber.

Lens/Objective	Collection efficiency
Olympus Plan Achromat x10 Objective	58%
Olympus Plan Achromat x4 Objective	65%
Thorlabs AC254-030-A F = 30 mm lens	65%
Thorlabs AC254-035-A F = 35 mm lens	65%
Thorlabs AC254-040-A F = 40 mm lens	57%

A maximum collection efficiency of 65% is obtained for three of the five lenses/objectives, which is sufficient for the experiments in this thesis. To further improve on the collection efficiency, a 1:1 telescope can be used to improve the spatial mode matching of the incoming and outgoing beam of the fiber. For the remainder of this thesis the Olympus Plan Achromat x4 Objective is used.

6

Purcell enhancement of NV centers in diamond

In this chapter the Purcell enhancement of NV centers in diamond is discussed. In the first section the cavity that is used for the remainder of the experiments is characterized. This includes measurements and calculations of the relevant geometric parameters, the expected Purcell factor and branching ratio into the ZPL. This is followed by a section on the detection of NV centers in the cavity. In the third section, the Purcell factor is determined with use of lifetime measurements. In the final section, microwave driving of the NV center is demonstrated with an optically detected magnetic resonance measurement.

6.1. Cavity Characterization

In this section the cavity used for the remaining experiments is the characterized. The sample used in the experiments is the same as used in [31], developed in the way as described in [37]. In short, the diamond membrane is irradiated with electrons and annealed at temperatures up to 1100 °C which creates stable and optically coherent NV centers in the membrane. Afterwards, the membrane is bonded to a plane mirror with embedded microwave strip lines and the central region is etched to a thickness of roughly 5-6 µm with a surface roughness of $\sigma_{DA} < 0.4$ nm [31]. The striplines are connected to a support PCB with wire bonds which allows for microwave spin control of the NV centers. An image of the sample is shown in Figure 6.1.

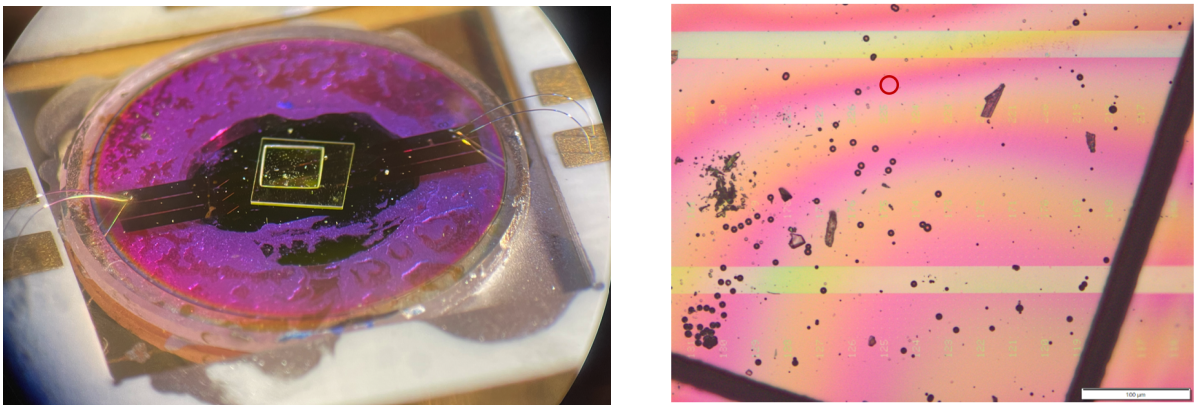

Figure 6.1: Images of the sample. Left: Image of the sample bonded on the flat mirror. The middle region of the sample is etched to a thickness of approximately 5-6 µm. One of the striplines is connected to a PCB with wire bonds. **Right:** Light microscope image of the sample. The black spots are contaminants and dirt on the sample which should be avoided. The red circle indicates the position of the cavity, close to the connected microwave stripline.

The fiber coating of the plane mirror with the bonded diamond membrane is different than the one discussed in Section 3.1. While the materials remain the same, the thickness of the SiO_2 layers are three times larger than the Ta_2O_5 layers. This results in a narrow stop band from $\lambda = 620 - 660$ nm with losses $\mathcal{L} \approx 400$ ppm. In addition, the refractive index before the mirror is no longer $n = 1$ from the air, but $n = 2.41$ from the diamond. This further increases the losses of the plane mirror to $\mathcal{L} \approx 900$ ppm, resulting in a maximally obtainable finesse of $\mathcal{F} \approx \frac{2\pi}{950 \cdot 10^{-6}} \approx 6600$, without considering scattering/absorption on the diamond-air surface.

Cavity parameters at 6 K

At low temperatures, the fiber tip mirror is moved into the thinned down part of the membrane to create a hybrid cavity. Multiple positions close to the striplines are checked by measuring the cavity linewidth to find a suitable cavity for the experiments. As shown in Figure 6.1, the sample is contaminated with dirt particles, which possibly originate from kapton tape used to hold the sample while etching. These spots should be avoided to not introduce additional losses to the cavity. A suitable spot for the cavity is found, indicated with a red circle in Figure 6.1. An image of the cavity spot is shown in Figure 6.2.

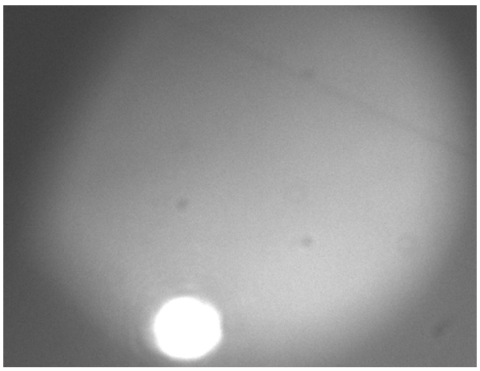

Figure 6.2: Image of the cavity spot. Image taken of the cavity spot by focusing the objective on the plane mirror. The fiber tip mirror emits green laser light to reveal the spot of the cavity on the membrane. The microwave stripline is visible on the top right corner, situated roughly 20 µm from the cavity spot.

The linewidth is measured with both a two-laser linewidth scan and sideband modulation. The results are shown in Figure 6.3. Next, the diamond thickness and air gap length of the cavity are obtained. This is done by measuring the transmission spectrum of the cavity with the spectrometer while sweeping the cavity length and fitting the fundamental modes to Eq.(2.29). The results are shown in Figure 6.4.

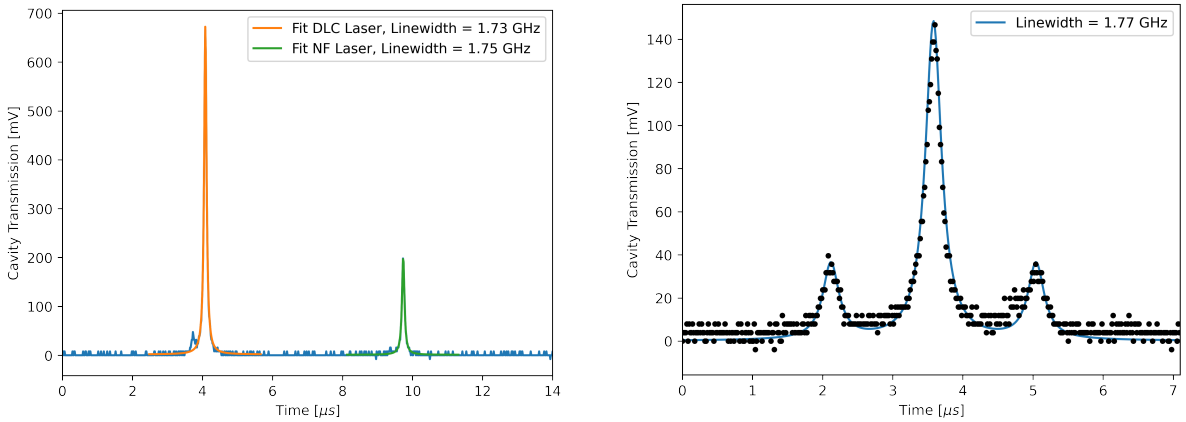

Figure 6.3: Linewidth measurements of the hybrid cavity. The linewidth is measured with a two laser linewidth scan (left) and sideband modulation (right). Transmission is measured while scanning the cavity length with $f \sim 3$kHz. Since the sideband modulation method is more accurate than the two laser linewidth scanning method, the measured linewidth of (1.77 ± 0.03) GHz is used in further calculations.

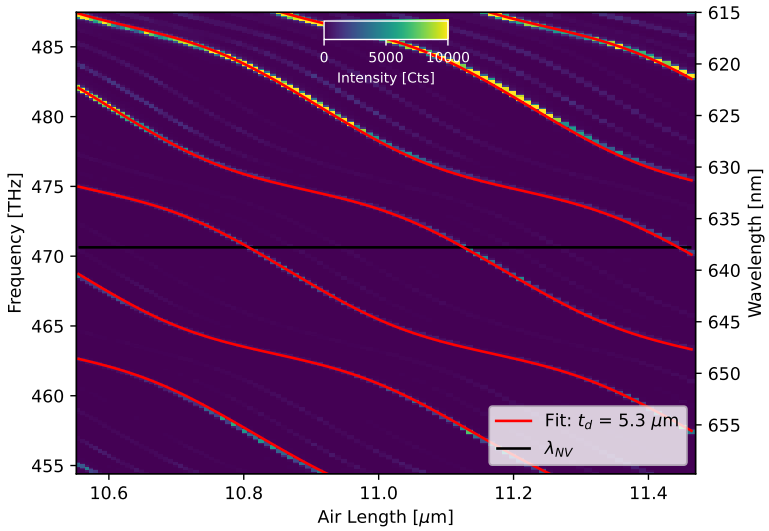

Figure 6.4: Hybrid cavity transmission spectrum with scanning the length. The cavity spectrum is measured with the spectrometer while sweeping the fine piezo voltage from -2 V to 10 V. The fundamental modes are fitted to Eq.(2.29) which shows very good agreement between theory and experiment. The fit results in a diamond thickness of $t_d = 5.3$ µm and air length $t_a = 10.8$ µm at the first mode overlap with the ZPL of the NV (indicated with a black horizontal line).

The measurements show that the cavity has a linewidth $\delta\nu = (1.77 \pm 0.03)$ GHz, diamond thickness $t_d = (5.3 \pm 0.1)$ µm and air length $t_a = (10.8 \pm 0.1)$ µm. More relevant cavity parameters are estimated with these numbers, assuming a $ROC = (21.4 \pm 0.1)$ µm of the fiber mirror. The results are shown in Table 6.1.

Table 6.1: Cavity parameter estimation results. Parameters are estimated with measured parameters $\delta\nu = (1.77 \pm 0.03)$ GHz, $t_d = (5.3 \pm 0.1)$ µm, $t_a = (10.8 \pm 0.1)$ µm and $ROC = (21.4 \pm 0.1)$ µm. F_P and β are calculated without considering vibrations. The simulations are based on the methods from [18].

Parameter	Value	Method
Radius of Curvature (ROC)	(21.4 ± 0.1) µm	Fiber dimple characterization
Linewidth ($\delta\nu$)	(1.77 ± 0.03) GHz	Measurement with sideband modulation
Diamond thickness (t_d)	(5.3 ± 0.1) µm	Measurement fitted to Eq.(2.29)
Air gap (t_a)	(10.8 ± 0.1) µm	Measurement fitted to Eq.(2.29)
Beam width (ω_0)	1.45 µm	Calculation using Eq.(2.42)
Mode volume (V_0)	108 λ^3	Numerical solution of Eq.(2.43)
Effective length (L_{eff})	16.8 µm	Numerical solution of Eq.(2.44)
Total losses ($\mathcal{L}_{\text{eff}}$)	3000 ppm	Calculation using Eq.(2.45)
Finesse ($\mathcal{F}$)	2100	Calculation using Eq.(2.45)
Quality factor (Q)	266000	Calculation using Eq.(2.13)
Expected Purcell factor (F_P)	13.4	Calculation using Eq.(2.51)
Branching ratio into ZPL (β)	0.29	Calculation using Eq.(2.56)
Outcoupling efficiency	30%	Calculation using Eq.(2.33)

Cavity vibrations estimation

The expected Purcell factor and branching ratio into the ZPL from Table 6.1 are calculated without considering vibrations. Measuring vibrations in a hybrid cavity is not as straightforward as for a bare cavity, since Eq.(5.1) does no longer hold due to the non-linear dispersion relation as shown in Fig (6.4). The dispersion relation is estimated by taking the slope of the spectrum of Fig (6.4) at the crossing of λ_{NV} and $t_a \sim 10.8$ µm, resulting in $|\Delta\nu/\Delta t_a| \approx 28.8$ MHz/pm.

Next, the contribution of the vibrations to the broadening of the linewidth is estimated. The previous linewidth is measured by scanning the cavity length with a frequency of 3 kHz, where additional broadening due to vibrations can be neglected. From this measurement it is known that the cavity

transmission has the form of a Lorentzian with linewidth $\delta\nu = 1.77$ GHz, and from Section 5.1 it is known that the vibrations in the cavity follow a Gaussian distribution. This results in a cavity transmission that follows the convolution of the cavity Lorentzian and the Gaussian of the vibrations, which is a Voight function. To extract the Gaussian contribution to the broadening, the transmission is fitted to a Voight function with a Lorentzian contribution fixed to $\delta\nu = 1.77$ GHz. The results are shown in Figure 6.5.

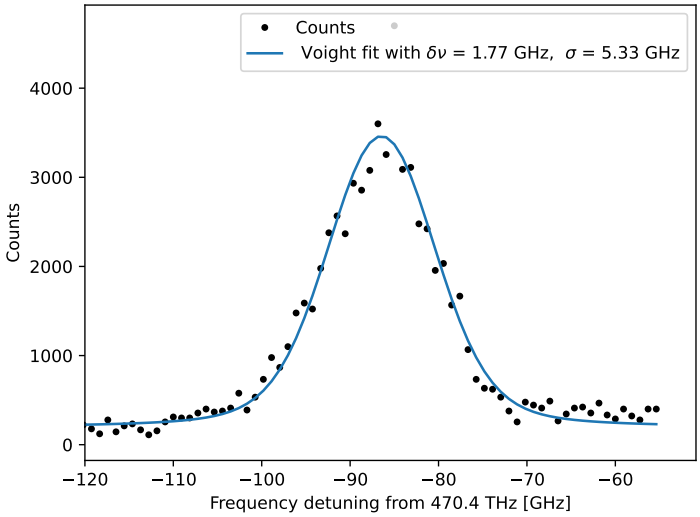

Figure 6.5: Voight fit of cavity transmission. The cavity is probed with the resonant lasers while sweeping the cavity length. Resonant laser 1 is frequency-stabilized to −85 GHz and the resonant laser 2 to 15 GHz w.r.t. 470.4 THz (not visible) to convert the fine scanning voltage to frequency. The transmission is measured in the ZPL path. The data is fitted to a Voight function with fixed Lorentzian contribution of $\delta\nu = 1.77$ GHz, resulting in a Gaussian contribution of $\sigma \approx 5.33$ GHz.

The Voight fit results in a Gaussian contribution of $\sigma \approx 5.33$ GHz. The RMS value of the vibrations is calculated with the dispersion relation, resulting in $\sigma_{RMS} = \sigma / \frac{\Delta\nu}{\Delta t_a} \approx 190$ pm. This is roughly an order of magnitude higher than the vibration measurements of the bare cavity (see Section 5.1). This increase of the vibrations is attributed to the mirror holder with the PCB and the microwave cables, as these where not present in the bare cavity configuration.

Next, the effect of the vibrations on the expected Purcell factor is calculated. The spectral overlap between the NV center and the cavity at detuning Δt_a is calculated with [18]:

$$\xi_s(\Delta t_a) = \frac{1}{1 + 4Q^2\left(\frac{\nu_{cav}(\Delta t_a)}{\nu_{ZPL}} - 1\right)}, \tag{6.1}$$

where $Q = \nu/\delta\nu$ is the quality factor of the cavity and ν_{cav} is the resonance frequency of the cavity at detuning Δt_a, which is calculated with $\Delta\nu/\Delta t_a$. The Purcell factor for a cavity at detuning Δt_a is calculated with $F_{P,\Delta t_a} = \xi_s(\Delta t_a) F_P$, where F_P is the Purcell factor at zero detuning.
Since the vibrations in the cavity follow a Gaussian distribution, the probability distribution of cavity detunings is:

$$P(\Delta t_a) = \frac{1}{\sqrt{2\pi\sigma_{vib}^2}} e^{-\frac{\Delta t_a^2}{2\sigma_{vib}^2}}, \tag{6.2}$$

where σ_{vib} is the RMS value of the vibrations. Combining this and integrating yields the average Purcell factor:

$$F_{P,avg} = F_P \int P(\Delta t_a)\xi_s(\Delta t_a) d(\Delta t_a). \tag{6.3}$$

The average Purcell factor is calculated numerically with the calculated expected Purcell factor $F_P = 13.4$ for $\sigma_{vib} \in (0, 250)$ pm. The results are shown in Figure 6.6.

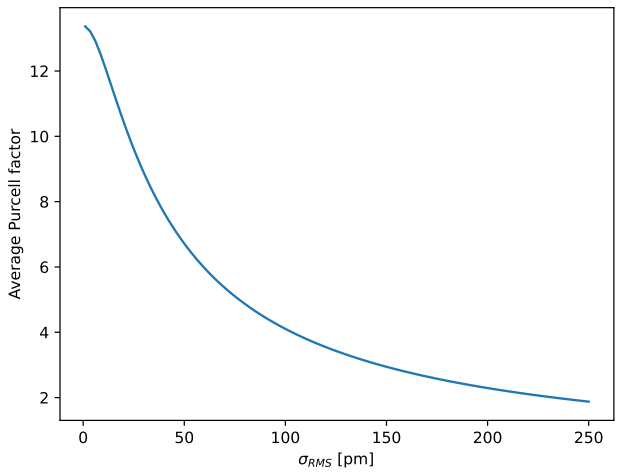

Figure 6.6: Simulated average Purcell factor with vibrations. The average Purcell factor is simulated by numerically solving Eq.(6.3) for $F_P = 13.4$ and $\sigma_{vib} \in (0, 250)$ pm.

Figure 6.6 shows that the expected average Purcell factor is highly depended on the vibrations in the cavity. The estimation of vibrations in the cavity with $\sigma_{RMS} \approx 190$ pm reduces the expected Purcell factor to $F_P \approx 2.4$.

6.2. Detecting NV Centers in the Cavity

The next step is to detect NV centers that are coupled to the cavity. To do this, the NV centers are off-resonantly excited with $\sim$ 3 mW continuous green laser power (measured after the cavity) while collecting emitted photons in the ZPL path. This is done while scanning the cavity close to the length corresponding to a resonance on the expected NV ZPL frequency at 470.4 THz. In addition, resonant lasers 1 and 2 are frequency-stabilized to a reference frequency on the borders of the scanning range and heavily attenuated to obtain a conversion factor from scanning piezo voltage to frequency. The results are shown in Figure 6.7.

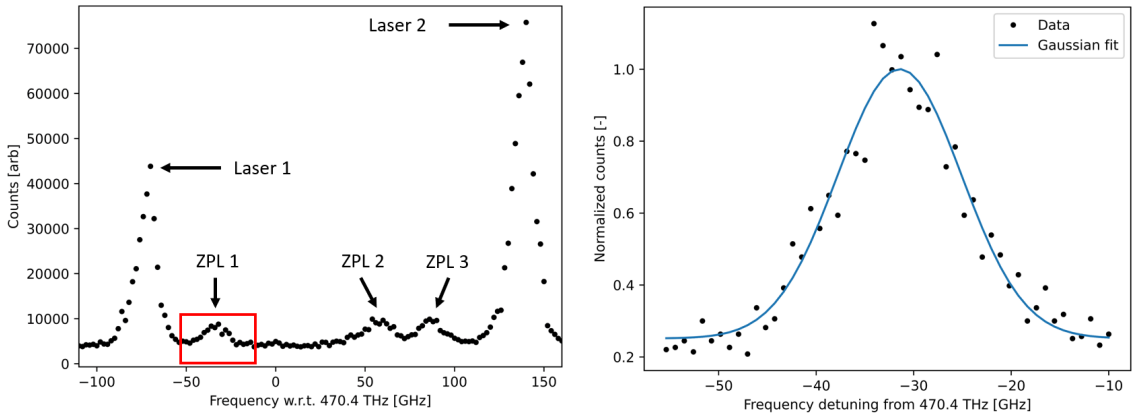

Figure 6.7: Off-resonant excitation collected in the ZPL path while sweeping the cavity length. The hybrid cavity is pumped with continuous green laser light while collecting in the ZPL path. **Left:** The cavity length is swept by applying piezo voltage steps of 1 mV in a range of 180 mV. The resonant lasers are used to obtain a conversion factor from piezo voltage to frequency. Laser 1 is frequency-stabilized to -75 GHz and resonant laser 2 is stabilized to 140 GHz w.r.t. 470.4 THz. The transmission reveals three distinct ZPL peaks, with ZPL 1 isolated from the others. This peak is used for further measurements. **Right:** zoomed in an normalised transmission peak of ZPL 1. The normalised counts are fitted to a Gaussian with $\sigma = 6.4$ GHz, $\delta\nu = 14.9$ GHz and center frequency $\nu = -31.4$ GHz.

Next, a photoluminescence (PL) measurement is done while sweeping the cavity length. Similar to the previous measurement, the NV centers are off-resonantly excited with $\sim$ 3 mW continuous green laser power but the emitted photons are now collected in the spectrometer path. The results are shown in 6.8

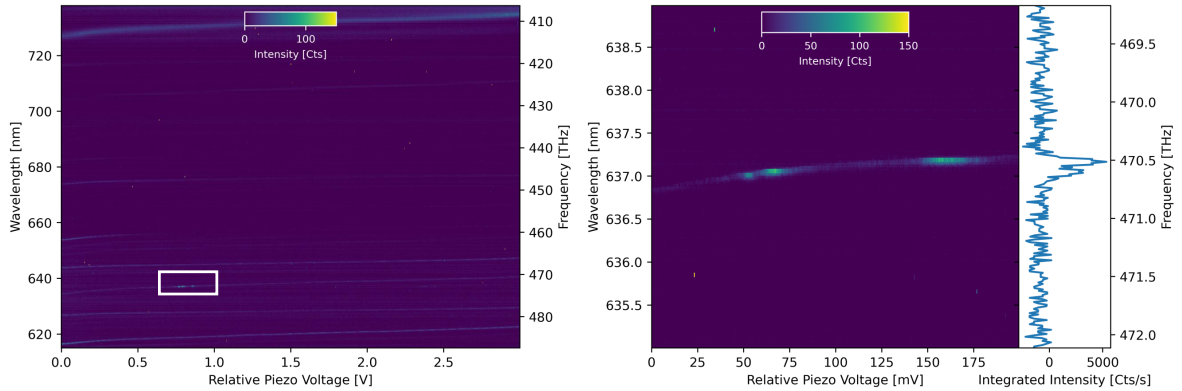

Figure 6.8: Photoluminescence measurement. The NV centers are off-resonantly excited with the green laser while sweeping the cavity length. The emission is collected in the spectrometer path. **Left:** The coarse grating of the spectrometer is used to measure over long range of wavelengths. The white square shows the three distinct ZPL peaks. **Right:** The fine grating of the spectrometer is used to image the three peaks with a higher resolution. The right inset shows the integrated intensities of the emission.

In the PL measurements the three ZPL peaks from Figure 6.7 are visible. In addition to the ZPL

emission, some cavity mode lines are visible for different wavelengths. For wavelengths $\lambda > 637$ nm the modes are attributed to cavity enhanced PSB emission and for $\lambda < 637$ nm the modes are attributed to cavity enhanced Raman scattering from the diamond membrane [38].

Both measurements show three distinct peaks, of which one is well-isolated (ZPL 1). This peak is used for the remainder of the experiments. Having detected this NV center in the cavity, the next step is to determine its coupling to the cavity by measuring the Purcell factor. This is discussed in the next Section.

6.3. Lifetime Reduction due to Purcell Enhancement

As previously discussed in Section 2.3, the Purcell effect adds an additional decay channel for the NV center which leads to a shorter excited-state lifetime. By measuring the lifetime with and without the cavity, the Purcell factor can be extracted.

The lifetime is measured with use of the pulsed green laser. The laser is set to ~ 3 mW (average power measured after the cavity) with a pulse frequency of 10 MHz. The laser is synced with the timetagger (HydraHarp), which counts the APD events of the ZPL. After each laser synchronization pulse, the timetagger records events for a time window of up to 100 ns. Once the APD detects a photon the timetagger saves the timestamp after the synchronization. This is repeated until the timetagger has registered at least 50.000 events to gain sufficient statistics. The background is measured by detuning the cavity far away (> 100 GHz) from the NV center. The following lifetime measurements are corrected for this by subtracting the background measurement, normalized with the number of events. An example is given in Figure 6.9.

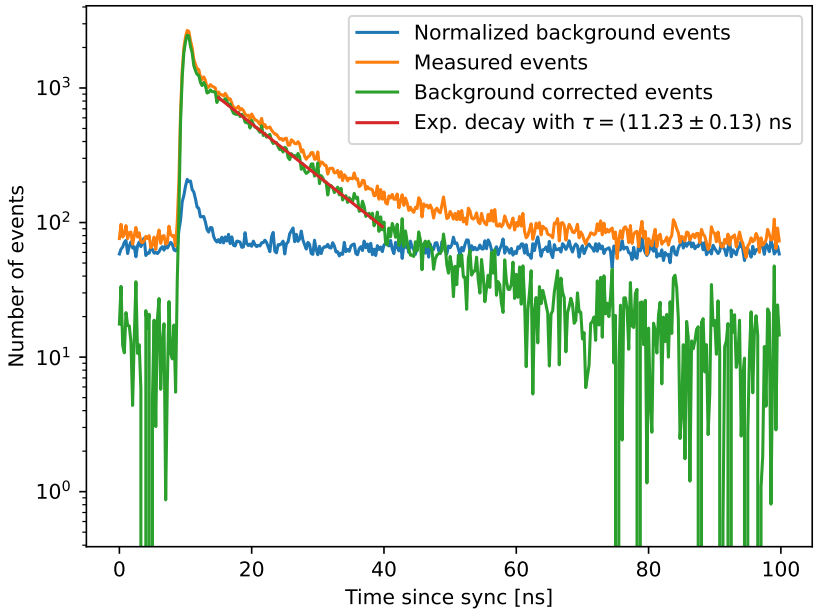

Figure 6.9: Lifetime measurement example. The timetagger measures at what time after the optical excitation pulse the APD measures a photon, which is repeated for > 50.000 times. A background measurement is done by fully detuning the cavity resonance frequency from the the ZPL emission of the NV, which is normalised and subtracted from the total measured events. The background corrected data is fitted what an exponential decay function in a time window of 15-40 ns to only include the NV emission in the calculation of the lifetime.

The lifetime is measured for different detunings between the NV center and the cavity resonance frequency. The lifetime of the NV center without the cavity is approximated by taking the lifetime for maximum detuning where the count rate is still above the background count rate. The results are shown in Figure 6.10.

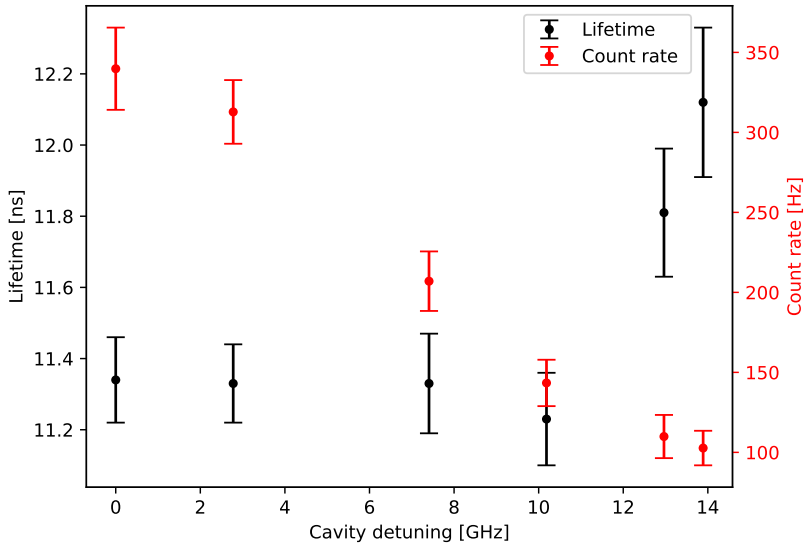

Figure 6.10: Excited-state lifetime measurements for different cavity detunings. The lifetime (shown in black) is measured for different detunings between the cavity resonance frequency and the frequency of the ZPL emission. The highest and lowest measured lifetimes are $\tau_{hom} = (12.12 \pm 0.21)$ ns and $\tau_{cav} = (11.23 \pm 0.14)$ ns respectively. The corresponding count rate from the cavity-coupled NV center is plotted in red, following the Gaussian-broadened linewidth.

Figure 6.10 shows the highest and lowest measured lifetimes are $\tau_{hom} = (12.12 \pm 0.21)$ ns and $\tau_{cav} = (11.23 \pm 0.14)$ ns respectively. The cavity off-resonant lifetime is comparable to lifetimes found in bulk diamond with solid immersion lenses and confocal microscope setups [13]. These values are used to calculated the Purcell factor with Eq.(2.55), which results in $F_P = 2.6 \pm 0.5$. This result is in good agreement with the calculated expected Purcell factor of $F_P \approx 2.4$. The branching ratio into the ZPL is calculated with Eq.(2.56), resulting in $\beta = 0.07 \pm 0.01$. This leads to the conclusion that coupling the NV center to the cavity increases both the branching ratio into the ZPL and the outcoupling efficiency by a factor of ~ 2, compared to state-of-the-art solid immersion lenses in confocal microscope setups [14].

6.4. Optically Detected Magnetic Resonance

With a NV center is coupled to the cavity, the next step to convert the setup to a quantum network node is to establish spin control. While full spin control is outside the scope of this thesis, the ability to drive the spin of the NV center can be tested with an optically detected magnetic resonance (ODMR) measurement.

By driving the NV center with microwaves with frequency equal to the zero-field splitting $D_{gs} = 2.88$ GHz, the $m_s = \pm 1$ states are partially populated. After these states are excited, parts of the excitation decay trough the long-lived ($\sim$ 370 ns [39]) singlet states without emitting ZPL photons, leading to a decreased count rate in the ZPL path (see Figure (2.2) for a detailed overview of the electronic structure of the NV center).

The ODMR measurement is prepared by setting the cavity on resonance with ZPL 1 while scanning the cavity length at 6 Hz with an amplitude of 100 mV. Scanning the entire cavity over the transmission peak ensures that the cavity does not go off resonance. The NV centers are excited off-resonantly with $\sim$ 3 mW green continuous laser light. The emission in the ZPL path is collected while sweeping the microwave driving frequency from 2.865 GHz to 2.895 GHz. The results are shown in Figure 6.11.

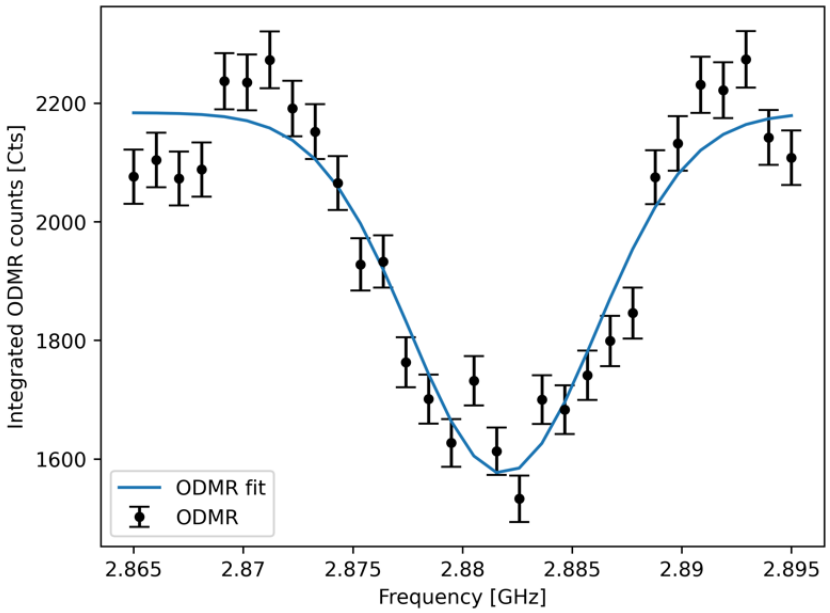

Figure 6.11: ODMR measurement. The microwave power is set to 25 dB and the driving frequency is swept from 2.865 GHz to 2.895 GHz in 30 steps. For one scan the ZPL emission is collected for 200 ms at each frequency step. The y-axis shows the integrated counts of multiple scans. The Gaussian fit results in a dip contrast of 28 ± 2 % with center frequency $D_{gs} = 2.882 \pm 0.001$ GHz. Error bars indicate the square root of the integrated counts.

The results show a measured zero-field splitting of $D_{gs} = (2.882 \pm 0.001)$ GHz with a contrast of (28 ± 2) %, marking the first ODMR measurement of an open microcavity-coupled NV center. This leads to the conclusion that the spin of the NV center can be driven with microwaves while coupled to the cavity, paving the way for spin control of cavity-coupled NV centers.

7

Conclusion and Outlook

The goal of this thesis is to simultaneously increase the branching ratio into the ZPL and the outcoupling efficiency of NV centers by coupling them to a Fabry-Pérot microcavity. To this end, fiber tip mirrors are characterized to optimize the finesse of the cavity. Four of the thirteen characterized fiber tip mirrors obtain a maximum finesse of $\mathcal{F} > 9500$, of which one is chosen for the remainder of the experiments. The vibrations in the bare cavity are analyzed, revealing a vibration level of $\sigma_{RMS} = 18$ pm for low coldhead settings and $\sigma_{RMS} = 22$ pm for high coldhead settings while operating at $T \sim 7.5$ K. This shows that the passive stabilization of the experimental setup performs excellent for the bare cavity configuration.

The setup is prepared for future research, which includes resonant excitation measurements. For this purpose, resonant laser scans are demonstrated as proof of principle. In addition, the achievable polarization suppression for filtering resonant excitation pulses from the emission of the NV centers is measured. A polarization suppression of ~ 30 dB is achieved, which is in combination with time filtering sufficient for spin-photon entanglement experiments [36].

The hybrid cavity is formed and characterized, resulting in a finesse $\mathcal{F} \approx 2100$, beam waist $w_0 \approx 1.45$ µm, quality factor $Q \approx 266000$, mode volume $V_0 \approx 108\ \lambda^3$, and outcoupling efficiency $\sim 30\%$. The vibrations in the hybrid cavity are measured, which results in $\sigma_{RMS} \approx 190$ pm. This value is roughly one order of magnitude higher than for the bare cavity configuration, which is attributed to the addition of the support PCB and microwave cables in the hybrid configuration. The expected Purcell factor for these vibrations is calculated, resulting in $F_P \approx 2.4$.

The NV centers in the cavity are detected by off-resonant excitation and sweeping the cavity length, while collecting the emission in both the ZPL path and spectrometer. Both measurements show three distinct ZPL peaks, of which one is well-isolated, which is used for the lifetime measurements. The lifetime measurements are done for multiple cavity detunings, where the highest and lowest measured lifetimes are $\tau_{hom} = (12.12 \pm 0.21)$ ns and $\tau_{cav} = (11.23 \pm 0.14)$ ns respectively. The cavity off-resonant lifetime is comparable to lifetimes found in bulk diamond with solid immersion lenses and confocal microscope setups. These values are used to calculate the Purcell factor, which results in $F_P = 2.6 \pm 0.5$. This result is in good agreement with the calculated expected Purcell factor of $F_P \approx 2.4$.

The branching ratio into the ZPL is calculated with the obtained Purcell factor , resulting in $\beta = 0.07 \pm 0.01$. This leads to the conclusion that coupling the NV center to the cavity increases both the branching ratio into the ZPL and the outcoupling efficiency by a factor of ~ 2, compared to state-of-the-art solid immersion lenses in confocal microscope setups [14].

The obtained results are similar to results of [31], where a Purcell factor of ~ 4 is reached on a similar experimental setup with a slightly better vibration level ($\sigma_{RMS} \sim 120$ pm). In [16], a Purcell factor of $F_P \sim 30$ is reached. Their experimental setup has two advantages over the setup discussed in this thesis. First, the cavity is operated in a helium-bath cryostat, which results in a vibration level of $\sigma_{RMS} < 10$ pm. Second, the authors state that the mirror coating of both mirrors have $\mathcal{L} < 100$ ppm,

which enabled a finesse of $\mathcal{F} > 10000$. While this greatly increases the achievable Purcell factor, using two very low-loss mirrors decreases the outcoupling efficiency of the cavity.

In preparation for further research on the setup, the ability to drive the spin of the NV center is tested with an optically detected magnetic resonance measurement. The results show a measured zero-field splitting of $D_{gs} = (2.882 \pm 0.001)$ GHz with a contrast of $(28 \pm 2)\%$. This leads to the conclusion that the spin of the NV center can be driven with microwaves while coupled to the cavity, paving the way for spin control of cavity-coupled NV centers.

Outlook

From the results of the vibration measurements it is clear that the current hybrid cavity configuration is not optimized in terms of vibration isolation. The Purcell factor would be greatly increased if a similar vibration level can be obtained for the hybrid configuration as for the bare configuration. In addition, finesse measurements in the room temperature setup demonstrate, that a finesse of $\mathcal{F} \approx 5000$ can be achieved on the sample used during this thesis. To show the influence of these parameters, the expected Purcell factor is simulated by numerically solving Eq.(6.3). The results are shown in Figure 7.1.

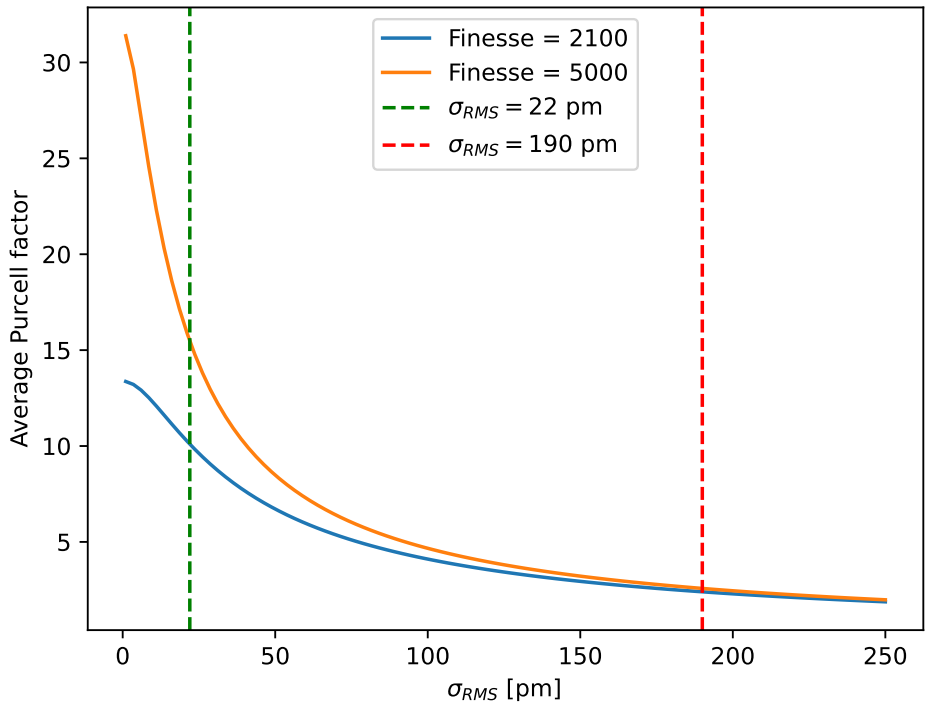

Figure 7.1: Expected Purcell factor for improved cavity parameters. The average Purcell factor is simulated by numerically solving Eq.(6.3) for $\mathcal{F} = 2100$ (blue) and $\mathcal{F} = 5000$ (orange).

By obtaining a vibration level of $\sigma_{RMS} = 22$ pm, the expected Purcell factor would increase to $F_P \approx 10.1$, resulting in a cavity branching ratio into the ZPL of $\beta \approx 0.23$. If a cavity is found with $\mathcal{F} = 5000$ for this vibration level, the Purcell factor would further increase to $F_P \approx 15.7$, corresponding to branching ratio of $\beta \approx 0.32$. The increase in finesse would also increase the outcoupling efficiency to $\sim 80\%$. Thus, by improving the cavity such that these realistic parameters are obtained, the branching ratio could be increased by a factor of ~ 10 and the outcoupling efficiency by a factor of ~ 5 compared to the current state-of-the-art implementation of solid immersion lenses in confocal microscope setups.

Bibliography

[1] S. Wehner, D Elkouss, and R Hanson. "Quantum internet: A vision for the road ahead". en. In: *Science* 362.6412 (Oct. 2018). Number: 6412, eaam9288.

[2] H. J. Kimble. "The quantum internet". en. In: *Nature* 453.7198 (June 2008). Number: 7198, pp. 1023–1030.

[3] J. I. Cirac et al. "Distributed quantum computation over noisy channels". In: *Physical Review A* 59.6 (June 1999), pp. 4249–4254.

[4] D. P. Nadlinger et al. "Experimental quantum key distribution certified by Bell's theorem". In: *Nature* 607 (2022), pp. 682–686.

[5] M. H. Abobeih et al. "One-second coherence for a single electron spin coupled to a multi-qubit nuclear-spin environment". In: *Nature Communications* 9 (2018), p. 2552.

[6] E. Togan et al. "Quantum entanglement between an optical photon and a solid-state spin qubit". en. In: *Nature* 466.7307 (Aug. 2010). Number: 7307, pp. 730–734.

[7] P. C. Humphreys et al. "Deterministic delivery of remote entanglement on a quantum network". en. In: *Nature* 558.7709 (June 2018). Number: 7709, pp. 268–273.

[8] C. E. Bradley et al. "A Ten-Qubit Solid-State Spin Register with Quantum Memory up to One Minute". en. In: *Physical Review X* 9.3 (Sept. 2019). Number: 3, p. 031045.

[9] M. Pompili et al. "Realization of a multinode quantum network of remote solid-state qubits". en. In: *Science* 372.6539 (Apr. 2021). Number: 6539, pp. 259–264.

[10] H. Bernien et al. "Heralded entanglement between solid-state qubits separated by three metres". en. In: *Nature* 497.7447 (May 2013). Number: 7447, pp. 86–90.

[11] S. D. Barrett and P. Kok. "Efficient high-fidelity quantum computation using matter qubits and linear optics". en. In: *Physical Review A* 71.6 (June 2005). Number: 6, p. 060310.

[12] C. Cabrillo, J. I. Cirac, et al. "Creation of entangled states of distant atoms by interference". In: *Phys. Rev. A* 59 (2 Feb. 1999), pp. 1025–1033.

[13] N. Kalb. "Diamond-based quantum networks with multi-qubit nodes". en. PhD thesis. Delft University of Technology, 2018.

[14] S. L. N. Hermans et al. "Qubit teleportation between non-neighbouring nodes in a quantum network". en. In: *Nature* 605.7911 (May 2022). Number: 7911, pp. 663–668.

[15] M. Ruf. "Cavity-enhanced quantum network nodes in diamond". en. PhD thesis. Delft University of Technology, 2021.

[16] D. Riedel et al. "Deterministic Enhancement of Coherent Photon Generation from a Nitrogen-Vacancy Center in Ultrapure Diamond". en. In: *Physical Review X* 7.3 (Sept. 2017). Number: 3, p. 031040.

[17] E. Janitz et al. "Cavity quantum electrodynamics with color centers in diamond". en. In: *Optica* 7.10 (Oct. 2020). Number: 10, p. 1232.

[18] S. van Dam et al. "Optimal design of diamond-air microcavities for quantum networks using an analytical approach". en. In: *New Journal of Physics* 20.11 (Nov. 2018). Number: 11, p. 115004.

[19] A. Faraon et al. "Coupling of Nitrogen-Vacancy Centers to Photonic Crystal Cavities in Monocrystalline Diamond". en. In: *Physical Review Letters* 109.3 (July 2012). Number: 3, p. 033604.

[20] B. Hensen et al. "Loophole-free Bell inequality violation using electron spins separated by 1.3 kilometres". en. In: *Nature* 526.7575 (Oct. 2015). Number: 7575, pp. 682–686.

[21] H. Bernien. "Control, measurement and entanglement of remote quantum spin registers in diamond". PhD thesis. 2014.

[22] S. van Dam. “Optical cavities, coherent emitters, and protocols for diamond-based quantum networks”. PhD thesis. Delft University of Technology, 2019.

[23] T. van der Sar. “Quantum control of single spins and single photons in diamond”. en. OCLC: 905868180. PhD thesis. Delft: Delft University of Technology, 2012.

[24] H. Kogelnik and T. Li. “Laser Beams and Resonators”. In: *Applied Optics* 5 (1966), pp. 1550–1567.

[25] B. E. A. Saleh and Malvin Carl Teich. *Fundamentals of Photonics, 2 Volume Set (Wiley Series in Pure and Applied Optics)*. English. Wiley, Feb. 20, 2019, p. 1520.

[26] J. Benedikter et al. “Transverse-mode coupling and diffraction loss in tunable Fabry–Pérot microcavities”. In: *New Journal of Physics* 17.5 (May 2015). Publisher: IOP Publishing, p. 053051.

[27] E. Janitz et al. “Fabry-Perot microcavity for diamond-based photonics”. In: *Phys. Rev. A* 92 (4 Oct. 2015), p. 043844.

[28] S. Nemoto. “Waist shift of a Gaussian beam by plane dielectric interfaces”. In: *Applied Optics* 27.9 (1988).

[29] D. J. Griffiths. *Introduction to Quantum Mechanics (2nd Edition)*. 2nd. Pearson Prentice Hall, Apr. 2004.

[30] L. Feije. “Active Length Stabilisation of an Open Fabry-Pérot Microcavity for Colour Centres in Diamond”. MSc thesis, Delft University of Technology (2021).

[31] M. Ruf et al. “Resonant Excitation and Purcell Enhancement of Coherent Nitrogen-Vacancy Centers Coupled to a Fabry-Perot Microcavity”. en. In: *Physical Review Applied* 15.2 (Feb. 2021). Number: 2, p. 024049.

[32] Y. van der Graaf. “Open Fabry-Pérot Microcavities for Color Centers in Diamond”. BSc thesis, Delft University of Technology (July 2023).

[33] D Hunger et al. “A fiber Fabry–Perot cavity with high finesse”. en. In: *New Journal of Physics* 12.6 (June 2010). Number: 6, p. 065038.

[34] F. Riehle. *Frequency Standards: Basics and Applications*. Wiley, 2003.

[35] Y. Herrmann et al. *Coherent Coupling of a Diamond Tin-Vacancy Center to a Tunable Open Microcavity*. 2023.

[36] R. Fang et al. *Experimental Generation of Spin-Photon Entanglement in Silicon Carbide*. 2023.

[37] M. Ruf et al. “Optically Coherent Nitrogen-Vacancy Centers in Micrometer-Thin Etched Diamond Membranes”. en. In: *Nano Letters* 19.6 (June 2019). Number: 6, pp. 3987–3992.

[38] D. Riedel et al. “Cavity-Enhanced Raman Scattering for In Situ Alignment and Characterization of Solid-State Microcavities”. In: *Phys. Rev. Appl.* 13 (1 Jan. 2020), p. 014036.

[39] L. Robledo et al. “Spin dynamics in the optical cycle of single nitrogen-vacancy centres in diamond”. In: *New Journal of Physics* 13 (2011).

A

Fiber Tip Mirror Characterization Example

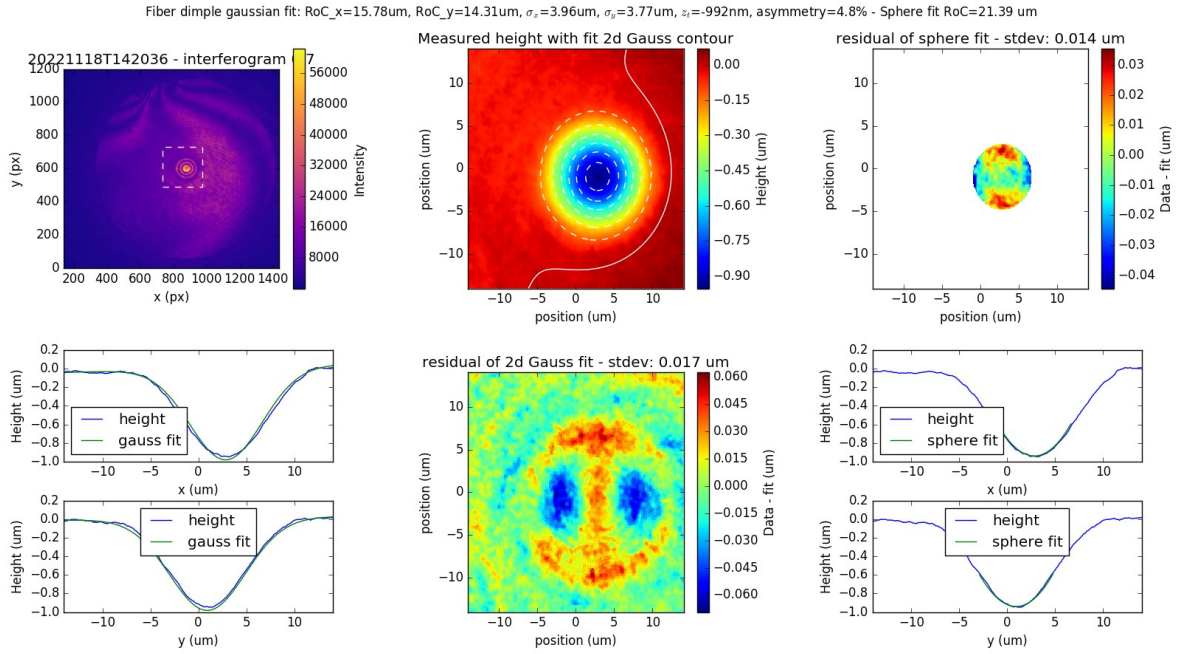

Figure A.1: Example of a fiber dimple characterization. The fiber dimple is characterized by taking a white light interferogram. A Gaussian fit is taken from the height profile in x- and y-direction, used to determine ROC_x, ROC_y and ellipticity of the dimple. A two-dimensional Gaussian fit is used to determine ROC_{sphere}, referred to in the text as ROC.

B

Bare and Hybrid Cavity Configurations

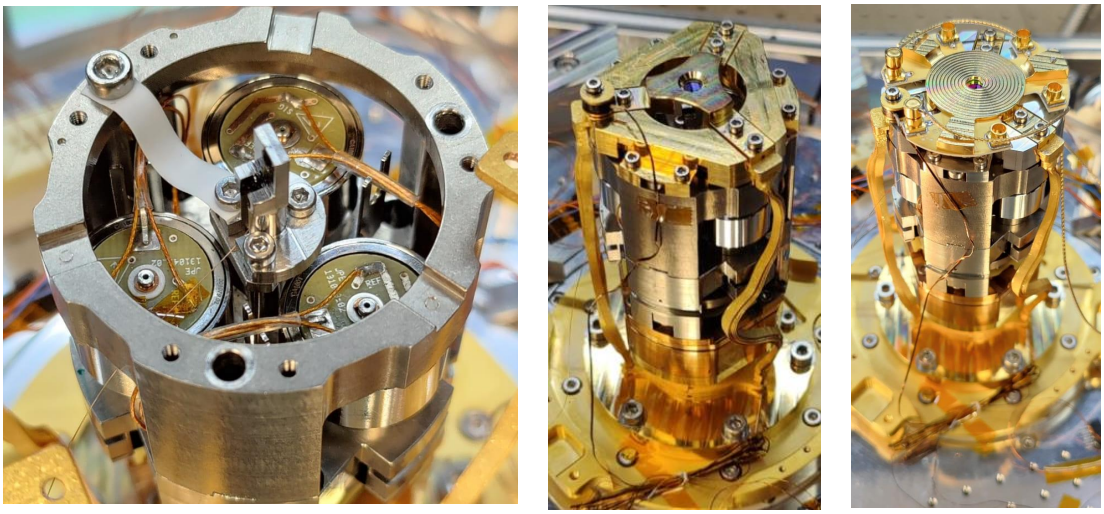

Figure B.1: Images of cavity configurations Left: Fiber holder inside the positioning system. The fiber holder is attached to a tripod system, which is moved with three linear actuators (the cylindrical electronics) **Middle:** The bare cavity configuration. **Right**: The hybrid cavity configuration. The thermal braids connect the mirror holder to the coldest part of the cryostat. The PCB is positioned underneath the circular mirror holder. The gold-plated microwave cables are connected to the PCB, visible on the left side of the mirror holder

C

Hybrid Cavity Mirror Holder with PCB

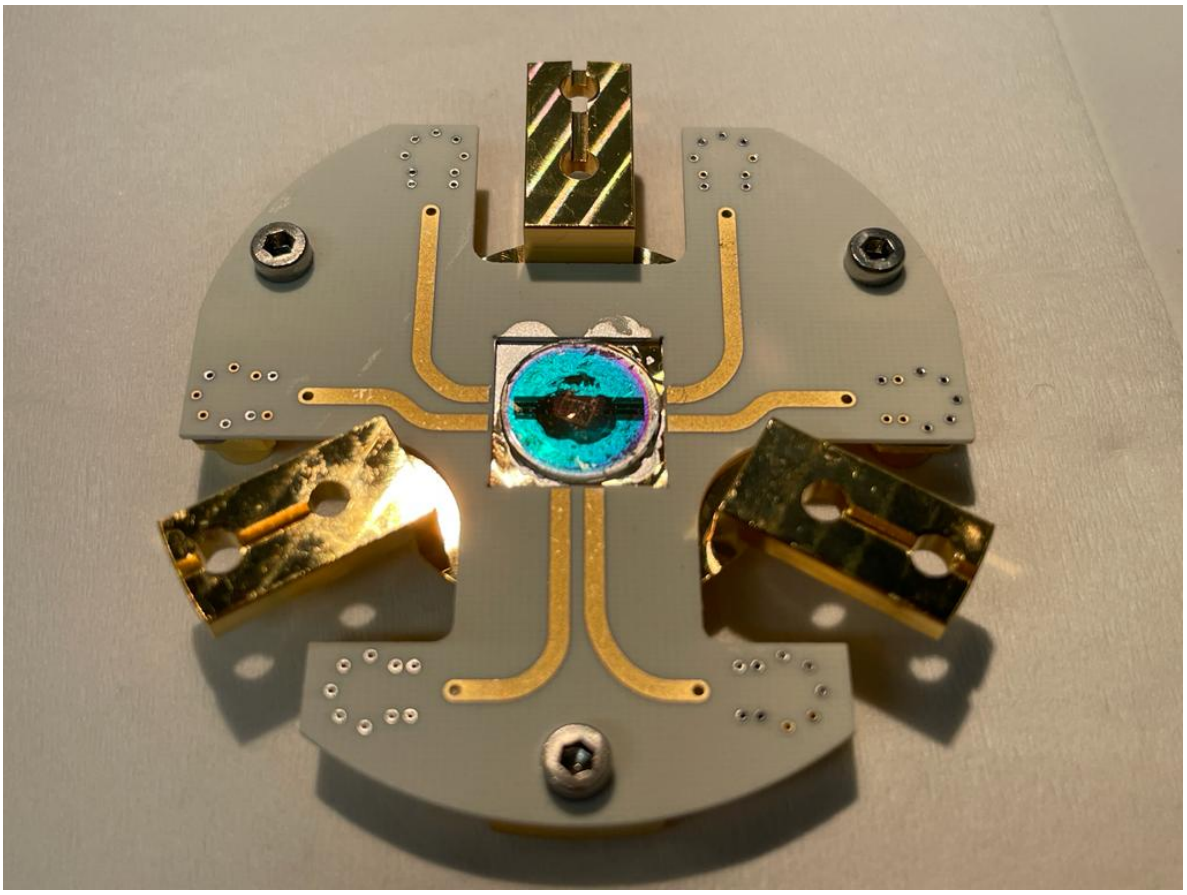

Figure C.1: Backside of the mirror holder with PCB. The sample is visible in the middle of the mirror. One of the striplines on the mirror is wire bonded to the PCB, which can be connected to microwave cables.